NGUYEN DINH CHAU[1], JADWIGA PIECZONKA[2], ADAM PIESTRZYŃSKI[3],
LE KHANH PHON[4], DUONG VAN HAO[5]

Rare earth elements in the Sin Quyen IOCG deposit, North Vietnam

Introduction

Four economic to sub-economic deposits (Sin Quyen, Muong Hum, Nam Xe and Dong Pao) with an above crustal-average-abundance of Cu, Au, Ag and REE have been identified in the North-West zone of Vietnam (Kušnir 2000; Pham et al. 2011). The Sin Quyen deposit is the largest iron oxide copper gold (IOCG) deposit in this area and is actively mined (Hitzman 2000). The copper grade in the ore ranges from 0.55 to 1.93%, and the abundance of iron ranges from a few percent up to several tens of percent (Zhao and Zhou 2011; Pham

✉ Corresponding Author: Adam Piestrzyński; e-mail: piestrz@agh.edu.pl

[1] AGH Unversity of Science and Technology, Kraków, Poland; ORCID iD: 0000-0003-1538-6658;
e-mail: cnd@agh.edu.pl

[2] AGH Unversity of Science and Technology, Kraków, Poland; ORCID iD: 0000-0002-3525-0996;
e-mail: jpieczon@agh.edu.pl

[3] AGH Unversity of Science and Technology, Kraków, Poland; ORCID iD: 0000-0001-6649-6772;
e-mail: piestrz@agh.edu.pl

[4] Hanoi University of Mining and Geology, Hanoi, Vietnam; e-mail: lekhanhphon humg@gmail.com

[5] Hanoi University of Mining and Geology, Hanoi, Vietnam; e-mail: haodnth@gmail.com

et al. 2011; Gas'kov et al. 2012). The ore reserves of this deposit are reported as 550,000 t Cu, 334,000 t REE, 843,000 t S, 34.7 t Ag and 25.3 t Au (Ta 1975; ESCAP 1990; McLean 2001; Ishihara et al. 2011). Since 2006, the deposit has been exploited with an open-cast system and the Fe- and Cu-concentrates are produced by magnetic and gravity flotation respectively. However, due to sulphur contamination, the Fe-concentrate is not economic. The annual production of over 30,000 tons of Cu, and approximately 300 kg Au as a co-product are reported, but REE have not been recovered.

The major ore bearing minerals identified in the deposit are magnetite, pyrite, pyrrhotite, chalcopyrite, cubanite, and sphalerite. Allanite, ilmenite, marcasite, tennantite, arsenopyrite and galena are accessory minerals, and native-Bi, bismuthinite, electrum, native gold, uraninite, and tellurides as minor constituents. The Sin Quyen deposit is interesting from a scientific point of view, since it consists of a complicated spatial distribution of various commodities and multi-crystalization stages as suggested by the results of absolute dating techniques (Ta 1975; Zhao and Zhou 2011; Ishihara et al. 2011). Due to the overlap of magmatic, hydrothermal and metamorphic processes resulting in several crystallization stages in the deposit, origin, ore crystallization, and relationships between the major and minor elements and mineralization are still being discussed (Ta 1975; McLean 2001; Pham et al. 2011; Ishihara et al. 2011; Hao et al. 2021). Allanite is the major REE carrier in the IOCG Sin Quyen deposit; bastnäsite, monazite and epidote are scarce. The REE-carrying minerals are dispersed but commonly occur in the deposit and are found in an assemblage with amphibole and epidote in massive ore (Gas'kov et al. 2012). According to McLean (McLean 2001) and Li and Zhou (Li and Zhou 2017), the first allanite population of mineralization was accompanied with Ca-K alteration (stage II), while the second population of allanites is related to the initial stage of the polymetallic ore precipitation of the polymetallic stage. The rocks hosting most magnetite and allanite as well as sulphide extend beyond the sulphide mineralization zones (McLean 2001). McLean (2001) also described in draft the view of two allanite populations; one is dark brown and more Fe rich, the other is younger, grayish in color and surrounding the older mineral as a rim. Li and Zhou (Li and Zhou 2017) and Li et al. (Li et al. 2018) reported that REE are also contained in monazite-(Ce) and chevkinite-(Ce) in the study deposit, but with subordinate abundance. In the deposit, LREE dominate with 692 ppm on average (McLean 2001; Ishihara et al. 2011; Pieczonka et al. 2015, 2017), while the average content of the HREE is 9 ppm. Optical investigation shows fine differences between two populations of allanites. Further study enables us to precisely determine the nature of these phases, and statistical elaboration helps facilitate geochemical quantitative processes. The aims of this paper are:

◆ to describe the two populations of allanite based on textural occurrence, their chemical composition including an apfu calculations;
◆ attempt to constrain the conditions of formation of the first population and second population of the allanites using $\delta^{34}S$ and other related minerals like uraninite and Cu-sulphides;
◆ characterize the principal REE currying minerals present in the deposit.

1. Geological setting

1.1. Regional geology

In North-West Vietnam, there are four structural units with a NW-SE orientation: the Red River zone, the Tule rift, the Da River zone and the Ma River shear zone (Figure 1). The Red River zone is dominated by Paleoproterozoic to Neoproterozoic-aged metamorphic and magmatic rocks including granitic gneiss, biotite-muscovite, and amphiboles (Tapponnier et al. 1990; Leloup et al. 2007; Faure et al. 2014). In this zone, the Phan Si Pan and Day Nui Con Voi (DNCV) belts, around 10 km thick and nearly 300 km long, form the south-east part of the Ailao Shan-Red River (ASRR) shear zone (Figure 1) (Tapponnier et al. 1990; Leloup et al. 2007). In the West, close to the Red River zone, there is the volcano-detrital basin Tu Le Rift bordering to the South with the Da River zone which is adjacent to the Song Ma shear zone. This zone joins to the NW with the Dien Bien Phu Fault (Figure 1).

The volcanic rocks in the Tu Le rift formed during two periods: in the Middle Jurassic (176–145 Ma) and the Late Cretaceous (80–60 Ma) (Roger et al. 2012). The main volcanic rocks in the Tu Le rift are Jurassic-Cretaceous rhyolite, trachyte and basalt, while gabbro, syenite, granosyenite and alkaline granite are minor. The Da River zone is interpreted as a continental rift dominated by Triassic terrigenous calcareous and sandstone. In these
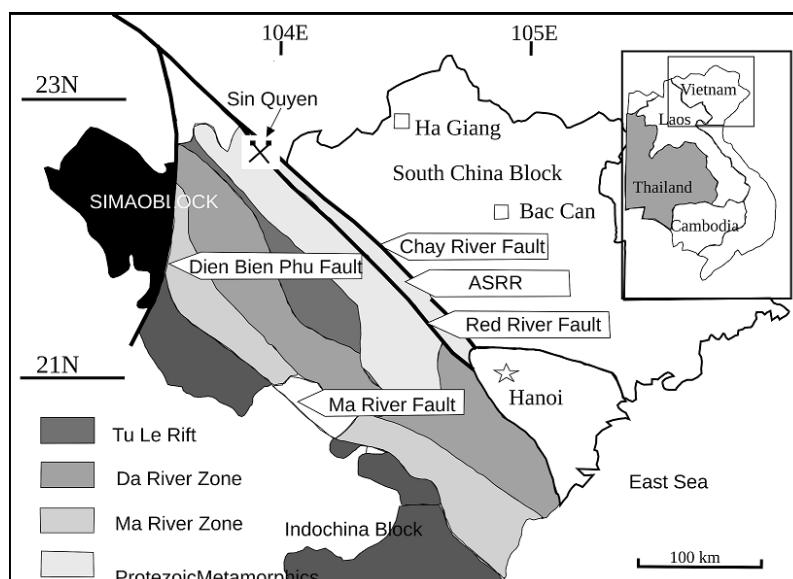

Fig. 1. Geological sketch of North-West Vietnam (Pham et al. 2011, modified)
with localization of the Sin Quyen deposit

Rys. 1. Uproszczona mapa geologiczna NW Wietnamu (Pham i in. 2011, ze zmianami)
z zaznaczoną lokalizacją złoża Sin Quyen

formations, some Permian rhyolite and tuff are interbedded. The Ma River zone consists of several northwest faults. This zone is built by Cambrian – Lower Ordovician metasediment Song Ma and Ham Rong Formations (Lepvrier et al. 2008). The Ma River zone is viewed as the boundary of the Indochina and South China blocks.

In North-West Vietnam, there are several Neo-Proterozoic and Late Permian and Early Triassic igneous formations. The metamorphic processes occurred in the Red River zone could be related to several magmatic intrusion and tectonic activities. The older Proterozoic intrusive suite (~750 Ma) comprises amphibolites and granitic gneiss, intruding both the Suoi Chieng and Sin Quyen formations (McLean 2001; Ishihara et al. 2011; Li and Zhou 2017; Li et al. 2018). This intrusive formation occurs as small lensoidal bodies in strike and dip with thicknesses of 10–100 meters. The Phan Si Pan Massif was formed by per-alkaline and meta-aluminous Perm-Triasic Po Sen-Hoa Binh plutons (253–251 Ma) (Carter and Clift 2008; Tong et al. 1996). These magmatic bodies intrude into the Suoi Chieng formation (Figure 2). In the Da River zone there is the occurrence of the Tu Le massif formed in the middle-late Jurassic (176–145 Ma) and late Cretaceous (80–60 Ma) (Tong et al. 1996; Carter and Clift 2008). The main tectono-metamorphic activity of the Ma River shear zone is the Indosinian orogeny at ~250 Ma (Tong et al. 1996; Liem et al. 2016).

The Day Nui Con Voi Belt appears as the elongated NW trending core of metamorphic rocks including garnet- biotite-sillimanite gneiss and garnet-biotite gneiss. This belt also consists of metamorphism amphibolite beds, migmatite, mylonite bands and small marble lenses (Liem et al. 2016). The rocks are strongly foliated. The foliation is parallel to the local trend of the gneiss core dipping near 70° to the NE.

The Phan Si Pan Belt is a high-grade metamorphic complex including the Suoi Chieng, Sin Quyen and Cam Duong formations. The Suoi Chieng Formation is composed of Paleoproterozoic biotite schist, amphibolite. This formation is conformably overlain by the Paleoproterozoic to Neoproterozoic-aged Sin Quyen metamorphosed formation with a thickness of nearly 1200 m. This formation is composed of gneiss, mica and graphite schists, marble lenses and volcanic rocks and intruded by several mafic intrusive dikes or lenses. Based on the mineral assemblage, the Sin Quyen Formation is divided into upper and lower units (McLean 2001; Gas'kov et al. 2012).

The lower unit is dominated by graphitic schist; however, in the upper unit is a lack of graphitic rock and gneiss prevails (Ta 1975; McLean 2001). The Sin Quyen upper formation is in contact in the fault with the Cam Duong Formation, which outcrops on the surface. This formation is composed of Cambrian sediments hosting apatite deposits (Ta 1975; McLean 2001; Gas'kov et al. 2012; Hao et al. 2021).

1.2. Deposit geology

The Sin Quyen copper deposit is hosted in the Upper Sin Quyen Formation and located 300 km north-west of Hanoi, 1 km from the Chinese border on the east bank of the Red

River. This deposit belongs to the iron oxide copper-gold (IOCG) type copper deposits. Mineralization occurs in lenses within an elongate NW trending zone which is 100–200 m wide, nearly 2.5 km long and extending in depth to around 500 m (Ta 1975).

1.2.1. General petrographic characteristics of the principal rocks occurring in the IOCG Sin Quyen deposit

In general, the Sin Quyen deposit consists of alternating leucocratic and melanocratic formations cut by lenticular quartz-feldspar pegmatoidal bodies and by quartz veins up to 40 cm thick. The leucocratic rock consists mainly of quartz (35–40%), K-feldspar (15–20%), acid plagioclase (20–25%) with porphyritic texture. The melanocratic rocks contain mainly dark coloured minerals: hornblende (65–70%), biotite (up to 15%), quartz (up to 35%), plagioclase (up to 30%), epidote (up to 45%) and allanite (1–3%). The quartz-amphibole-epidote rock is subordinate and occurs only within the ore hosting member. The rock is built of epidote (35–45%), amphibole (10–20%), and quartz (up to 20%). The main specific feature of this rock is a high allanite with 5 to 7% (Ta 1975; McLean 2001). This mineral occurs in assemblage with metamorphic minerals. It concentrates basically in amphibolites, where it is found in an assemblage with amphibole and epidote. Siltstone, gneiss and metamorphic skarn as metamorphosed sedimentary and gabro-amphibole, granite gneiss, porphyry granodiorite, porphyry granite and porphyry syenite as intrusive rocks are dominant in the study region.

1.2.2. Main characteristics of the ore bodies

The main mineralization zone is strongly deformed with fractured and dislocated gneiss, mica schist and clay matrix breccia. The gneiss is principally composed of biotite, feldspar

Fig. 2. Mining section with position of the ore body (black rocks) marked with red lines
(view towards NW, photo 2014)

Rys. 2. Ściana eksploatacyjna, czerwone linie wyznaczają granice ciał rudnych
(widok w kierunku NW, fot. 2014)

and quartz, the main composition of mica schist is biotite, muscovite, quartz and feldspar. In the mineralization zone, there are some Proterozoic granite dykes. The intrusive suites are barren of ore and basically consist of albite, biotite, and quartz (McLean 2001). The deposit is comprised of seventeen lensoidal ore bodies, striking NW-SE, dipping nearly vertically (70–90°), several to tens of meters thick (Figure 2), and up to a few hundred meters long. The following types of ore occur in the deposit: massive, banded, breccia cement and dispersed. Spatial distribution of Fe, Cu and REE is highly variable. From the ore geology point of view, the deposit is divided into two zones. The first zone is principally located in the central and eastern parts, and the main minerals are chalcopyrite, pyrrhotite and pyrite, which constitute nearly 90% of the ore composition with broad variations in the content of different sites. The second zone dominates in the western part; its principal minerals are magnetite, pyrite, chalcopyrite and pyrrhotite. The minerals contain from a few percent to 50% or more of ore composition. In the study deposit, allanite is the major carrier mineral for REE; bastnäsite, apatite and monazite are scarce (Ta 1975; McLean 2001; Gas'kov et al. 2012). Titanite, epidote and uraninite are also REE-bearing minerals (Pieczonka et al. 2019).

2. Samples and analytical methods

2.1. Sampling

The samples used encompass a broad range of geological materials available in the study area, from the different sulphide by the skarn, massive and breccia ores up to Cu, Fe concentrate and ore enrichment waste. A short description of some of the samples is presented in Table 1. The coordinate locations of the samples were determined using a Garmin 60CSx GPS, with an accuracy of ± 2–3 m and are shown in Figure 3. From the spatial distribution of view, thirty-four samples are representative of all zones in the deposit. Samples M1–M8 were collected from the central part, samples N1–N12 from the northern part and S1–S9 from the southern part.

2.2. Textural and compositional analysis

Analyses of ore minerals were carried out using a petrographic microscope with reflected light and a FEI Quanta-200 FEG scanning electron microscope at 20 kV acceleration equipped with an EDS detector located at the laboratories of the Faculty of Geology, Geophysics and Environmental Protection AGH University of Science and Technology in Kraków, Poland (FGGEP AGH-UST).

Bulk chemical analyses were carried out at ACME Laboratories in Vancouver Canada using the AQ251 method. A sample of 0.5 g was digested in Aqua Regia at 90°C, followed
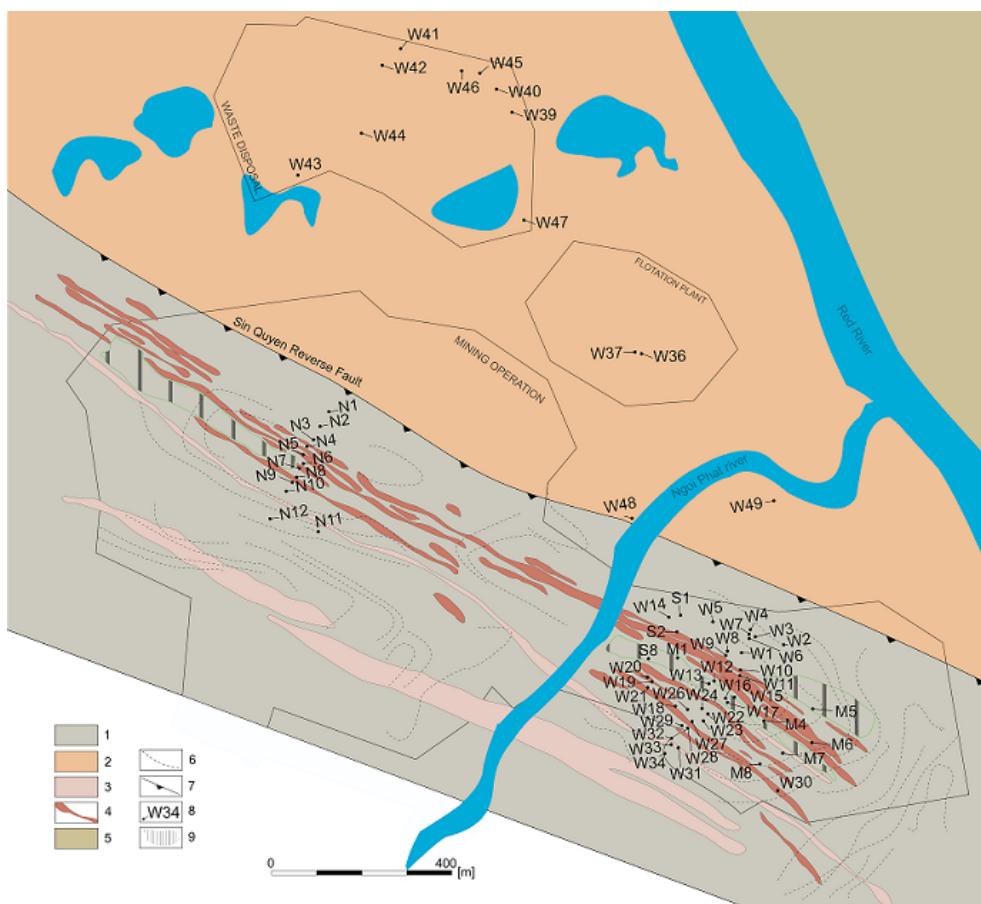
Fig. 3. Geological map of the Sin Quyen deposit with the location of the collected samples
(based on Ishihara et al. 2011 and Gas'kov et al. 2012)
1 – leucocratic biotite, plagioclase, K-feldspars –quartz, Paleo Proterozoic sequence, 2 – Cambrian
metasedimentary rocks, 3 – biotite granite and granodiorite, 4 – orebody, 5 – metamorphic sequence,
6 – topographic lines, 7 – fault and deep direction, 8 – sampling, 9 – alteration zone

Rys. 3. Mapa geologiczna złoża Sin Quyen z lokalizacją pobranych próbek
(na podstawie Ishihara i in. 2011 oraz Gas'kov i in. 2012)
1 – biotyt leukokratyczny, plagioklaz, K-skalenie-kwarc, następstwo Paleo-Proterozoiczne,
2 – Skały osadowe Kambryjskie, 3 – granit biotytowy i granodioryt, 4 – ciała rudne,
5 – skały metamorficzne, nierozdzielone, 6 – izolinie topograficzne, 7 – uskoki i kierunki upadu,
8 – lokalizacja próbek, 9 – strefy przeobrażone

by ICP-MS. A detailed description of the analytical methodology, detection limits, and uncertainties can be downloaded from the ACME Laboratories website at www.acmelab.com. Analytical uncertainties are typically 5% for most of the analyzed elements. The detection limit for REEs varies from 0.02 ppm to 0.5 ppm, and for U and Th, it is equal to 0.1 ppm.

2.3. REE analyses in allanites

Quantitative analyses were carried out at the Critical Elements Laboratory of the FGGEP AGH-UST using a JEOL SQ8200 electron-probe micro-analyzer (EPMA). For the principal elements, the following measurement lines and standards were used: SiKα (albite), AlKα (kyanite), SKα (anhydrite), UMβ (UO_2), YLα (YPO_4), PKα(YPO_4), ScKα (100%), TiKα (rutile), CeLα ($CePO_4$), LaLα ($LaPO_4$), ThMα (ThO_2), CaKα (wollastonite), PrLβ (PrPO4), TbLα ($TbPO_4$), DyLα ($DyPO_4$), ErLα ($DyPO_4$), LuLα ($LuPO_4$), GdLβ ($GdPO_4$), PbMα (crocoite), NdLα ($NdPO_4$), SmLα ($SmPO_4$), EuLβ ($EuPO_4$), TmLα ($TmPO_4$), YbLα ($YbPO_4$), HoLβ ($HoPO_4$), AsLα (InAs). Overlap corrections of Nd-Ce, Sm-Ce, Lu-Dy, Dy-Eu, U-Th, Tm-Sm, Gd-Ho were carried out using the method described by Pyle et al. (Pyle et al. 2002). The EPMA was operated in the wavelength-dispersion mode at an accelerating voltage of 15 kV, and a probe current of 40 nA, with a focused beam diameter of 3 μm. The peak/background counting times (s) were as follows: Si 10/5, Al 10/5, S 20/10, U 120/60, REE 45/15, P 20/10, Ti 20/10, Th 120/60, Ca 20/10, Pb 180/90, V 10/5, Fe 20/10 and As 20/10. The peak/ /background counting time for all members of the REE of the epidote sub-group was 50/20. This allowed a reduction in the level of detection twice. The Jeol ZAF matrix correction procedure was used during the final quantification of all analyzed elements.

The Raman spectroscope DXR AIY1100618 was used for determining the chemical composition and comparing the two populations of allanites. The sample was irradiated by monochromatic photons of 532 nm generated from an argon ion laser with 10 MW of power. The chemical compositions of the studied samples were identified and determined using the Raman spectra library.

2.4. Estimation of ore crystallization temperature using sulphur isotopes

Using sulphide $\delta^{34}S$ isotopes data provided by Seal (Seal 2006), crystallization temperature was calculated. The main factors controlling the magnitude of equilibrium sulphur stable isotope fractionations are temperature, chemical composition, and crystal structure and pressure (Ohmoto and Rye 1979; Dupuis and Beaudoin 2011). For the crustal condition, temperature and chemical composition are the most important, but the effect of pressure is minimal.

For sulphides occurring in the Sin Quyen IOCG deposit, the measured values of $^{34}\delta S$ are 8.65 ‰ and 8.27‰ for chalcopyrite and pyrrhotite, respectively (Pieczonka et al. 2019). Therefore, $\Delta_{ch\ py} = 0.38‰$. Using obtained $^{34}\delta S$ of pyrrhotite and chalcopyrite (Pieczonka et al. 2019) and following the work of Ohmoto and Rye (Ohmoto and Rye 1979), the calculated crystallization temperature was 355°C. This calculated temperature fits well in the range of 350°C to 400°C, which is related to sulphide minerals in the magmatic hydrothermal system (Hezarkhani et al. 1999; Landtwing et al. 2005) and statistical data coincides with that determined by Li and Zhou (Li and Zhou 2017).

3. Results

3.1. Geochemistry of the host rock and ore

The host rock and ore include interbedded gneisses composed of biotite – quartz and feldspar – biotite – muscovite; quartz and feldspar mica schists; metasomatites and amphibolites, which host the mineralization, and marbles (McLean 2001). The copper concentration ranges from several tens of ppm to more than 10.0 wt% (Appendix 1) with an average of 2.56 wt% in the deposit. The iron content ranges from a single percent up to 40.0%, and reflects the combined Fe content in magnetite, silicates, pyrite and chalcopyrite. The following metal concentrations values are below 100 ppm (Appendix 1): Zn, Pb, Co, Ni, Mo, Sb and Se. The concentrations of Au and Ag are highly variable. Gold in the ore and rock samples ranges from a single ppb up to 18.5 ppm with an average of 1.66 ppm. Silver concentrations range from 8 ppb to 4.650 ppm, with an average of 1.16 ppm (Appendix 1). High Au and Ag contents are commonly associated with massive copper ore characterized by high Cu concentration, suggesting an association of native gold with chalcopyrite and pyrite (Appendix 1). This regular is also confirmed by very high amounts of Au and Ag in the Cu concentrates (Appendix 1). The high content of sulphur is also observed in both Cu and Fe concentrates (Appendix 1), suggesting a similarity in the geochemical property of sulphur to that of Cu and Fe not only during the geological formation but also during the enrichment processes. In some ore samples, coarse crystalline titanite have been identified, but all samples are characterized by low concentrations of Ti (Appendix 1). The low amount of Ti is typical for IOCG deposits (Fengli et al. 2014; Chen et al. 2015; Li and Zhou 2018). The REE element analyses in rock chip samples show elevated values in the samples with economic copper concentrations (Appendix 1 and Table 1). Only three of the thirty-four ore samples analyzed have REE values greater than 0.2 wt% (Table 1). The average content of the ΣLREE is 692 ppm (for n = 34; Table 1), while that of ΣHREE is 9 ppm (Table 1). The patterns of REE for host rocks and ores are presented in Figure 4. Generally, the REE occur in all the host rocks and ore with different proportions, but all the studied materials are rich in LREE. The blue line of samples is relatively rich in the HREE (Figure 4). The yellow group of analyzed samples mostly represents massive ore and shows higher concentration of LREE. The behavior of Eu is also varied, even for the samples of one type; one sample is negative but another is positive, suggesting the crystallization conditions in the deposit were very diverse. The statistical correlation between the elements and a detailed discussion have been presented in our previous publication (Hao et al. 2021a). The REE concentration in both Fe and Cu concentrates are within the range of that found in rocks and raw ore material (rf. W36, W37, Table1); however, the wastes are significantly richer in REE, suggesting that most of the REE contents are removed during the Fe and Cu enrichment processes to the waste (W39, W40, W44, Table 1).

Table. 1. REE bulk chemical analyses of host rocks and Cu, Fe ore, concentrates and wastes (ppm)

Tabela 1. Zawartości metali REE w skałach otaczających, rudach Cu i Fe oraz w koncentratach Cu, Fe i odpadach (ppm)

Elements	La	Ce	Pr	Nd	Sm	Eu	Gd	Tb	Dy	Ho	Er	Tm	Yb	Lu	ΣLREE	ΣHREE	ΣREE	Marks
MDL	0.02	0.1	0.02	0.02	0.02	0.02	0.02	0.02	0.02	0.02	0.02	0.02	0.02	0.02	0.02	0.02	0.02	–
M1	169.2	237.3	21.44	50.83	4.12	1.78	1.83	0.18	1.21	0.25	0.73	0.16	1.14	0.14	486.5	3.81	490.31	Ep-amph. rock. Cu-Fe ore
M2	767	1110.7	91.3	242.48	18.48	6.85	8.45	0.90	4.40	0.83	2.09	0.38	2.20	0.30	2245.26	11.10	2256.36	Ep-amph. rock. Cu ore
M3	366	522.1	47.05	112.23	12.19	8.25	9.59	1.91	13.82	3.06	9.98	1.77	12.26	1.58	1077.41	44.38	1121.79	Ep-Am rock
M4	230.4	353.5	31.52	78.51	6.77	1.40	2.29	0.29	1.74	0.32	0.90	0.17	1.13	0.13	704.39	4.68	709.07	massive Cu-Fe ore
M5	463.7	685.9	59.93	150.22	11.87	2.40	4.18	0.61	3.34	0.70	2.24	0.39	2.60	0.39	1378.2	10.27	1388.47	Cu-Fe ore
M6	208.5	314.1	27.58	63.45	4.88	1.55	1.87	0.3	1.64	0.35	1.12	0.18	1.32	0.19	621.93	5.10	627.03	Bt-amph. rock.Cu ore
M7	48.9	71.7	6.34	15.62	1.67	0.49	0.69	0.1	0.79	0.15	0.51	0.09	0.59	0.11	145.41	2.34	147.75	massive Fe ore
M8	72.8	103.1	9.58	24.17	2.44	0.65	1.42	0.2	1.39	0.3	1.02	0.16	1.41	0.27	214.16	4.75	218.91	massive Cu-Fe ore
N1	464.3	710.5	67.1	187.38	20.49	4.76	11.93	1.63	9.77	1.86	5.67	0.95	5.38	0.64	1466.46	25.9	1492.36	Ep-Qtz-Pl rock
N2	171.8	273.1	27.72	80.90	11.49	2.3	8.14	1.31	7.81	1.49	4.35	0.64	3.65	0.41	575.45	19.66	595.11	carbonate-Qtz rock
N3	315.4	488.1	41.55	102.41	8.10	2.07	3.54	0.42	2.22	0.42	1.19	0.2	1.32	0.18	961.17	5.95	967.12	skarn
N4	228.1	334	29.9	69.51	5.99	1.18	3.64	0.46	2.67	0.55	1.52	0.27	2.02	0.30	672.32	7.79	680.11	Bt-amph. rock. Cu ore
N5	272.7	417	38.04	91.91	7.51	1.66	3.50	0.47	2.54	0.46	1.48	0.26	1.70	0.29	832.32	7.20	839.52	Bt-Ep rock. Cu-Fe ore
N6	197.6	302.3	29.62	80.77	8.54	1.95	4.86	0.66	3.89	0.76	2.17	0.32	2.07	0.29	625.64	10.16	635.8	Cu-Fe ore
N7	61.1	89.0	8.01	21.53	2.19	0.48	1.50	0.24	1.41	0.36	1.11	0.18	1.25	0.22	183.81	4.77	188.58	Cb-Qtz rock. Cu ore
N8	42.2	61.7	5.54	13.78	1.65	0.26	0.96	0.16	1.36	0.28	0.93	0.17	1.01	0.15	126.09	4.06	130.15	Bt-Qtz-amph. rock Cu ore
N9	51.2	82.8	8.12	24.62	2.97	0.77	2.24	0.35	2.07	0.5	1.47	0.25	1.85	0.28	172.72	6.77	179.49	amphibolite
N10	48.0	77.2	7.11	18.68	1.79	0.45	1.13	0.18	1.22	0.27	1.03	0.2	1.40	0.21	154.36	4.51	158.87	amphibolite Cu ore
N11	96.9	141.2	12.99	34.32	3.55	1.02	2.16	0.31	2.06	0.45	1.35	0.22	1.49	0.23	292.14	6.11	298.25	Massive Cu ore
N12	158.4	234.8	21.2	53.40	4.66	0.78	1.57	0.23	1.12	0.23	0.7	0.11	0.78	0.10	474.81	3.27	478.08	Ep-Am rock. Cu-Fe ore
S1	143.9	211.2	18.72	41.91	3.42	0.85	1.06	0.14	0.85	0.16	0.53	0.08	0.64	0.09	421.06	2.49	423.55	Bt-Am schist

Elements	La	Ce	Pr	Nd	Sm	Eu	Gd	Tb	Dy	Ho	Er	Tm	Yb	Lu	ΣLREE	ΣHREE	ΣREE	Marks
S2	215.5	326.0	29.66	75.06	6.17	1.01	3.02	0.34	1.72	0.36	1.08	0.19	1.06	0.18	656.42	4.93	661.35	Cu-Fe ore
S3	51.9	83.1	8.57	25.64	4.44	1.01	2.53	0.42	2.35	0.5	1.38	0.2	1.38	0.19	177.19	6.42	183.61	massive Cu-Fe ore
S4	557.1	833.7	75.64	196.2	17.95	3.69	9.80	1.19	5.82	1.22	3.44	0.47	3.20	0.44	1694.08	15.78	1709.86	massive Cu-Fe ore
S5	437.2	662.9	58.34	141.44	10.27	1.86	4.08	0.45	1.91	0.34	1	0.16	1.14	0.18	1316.09	5.18	1321.27	Cu-Fe ore
S6	831.7	1230.9	103.91	257.2	19.27	3.64	8.00	0.74	3.28	0.57	1.69	0.31	2.01	0.3	2454.62	8.90	2463.52	massive Cu-Fe ore
S7	42.2	76.4	8.64	29.07	5.42	0.83	4.20	0.54	2.88	0.52	1.24	0.19	1.11	0.17	166.76	6.65	173.41	carbonate-Qtz rock
S8	464.4	682.4	59.03	141.72	10.47	1.67	4.12	0.44	1.92	0.39	1.11	0.18	1.34	0.21	1363.81	5.59	1369.4	massive Cu-Fe ore
S9	417.1	618.4	53.93	131.1	9.97	1.81	3.55	0.42	1.98	0.36	1.05	0.18	1.14	0.18	1235.86	5.31	1241.17	Cu-Fe ore
W-15	13.1	19.13	3.24	11.09	2.36	0.68	1.89	0.40	2.05	0.45	1.62	0.25	2.1	0.47	51.49	7.34	58.83	ore from open pit
W-18	79.2	115.63	11.85	27.62	2.52	0.52	1.40	0.26	1.30	0.26	0.72	0.12	0.79	0.11	238.74	3.56	242.3	massive ore
W-25	43.1	62.92	12.98	47.01	10.58	3.74	8.31	1.46	8.93	1.9	5.28	0.88	5.38	0.72	188.64	24.55	213.19	quartz amph rock
W-31	31.2	45.55	7.67	25.95	5.45	1.8	4.11	0.86	5.90	1.42	5.11	0.81	5.72	0.89	121.73	20.71	142.44	skarn
W-31a	5.2	7.59	1.08	3.62	0.77	0.17	0.82	0.17	0.84	0.19	0.61	0.10	0.44	0.08	19.25	2.43	21.68	skarn with garnet
Min.	5.20	7.59	1.08	3.62	0.77	0.17	0.69	0.10	0.79	0.15	0.51	0.08	0.44	0.08	19.25	2.34	21.68	
Max.	831.70	1230.90	103.91	257.20	20.49	8.25	11.93	1.91	13.82	3.06	9.98	1.77	12.26	1.58	2454.62	44.38	2463.52	
Av.	228.44	340.76	30.73	78.57	7.37	1.89	3.89	0.55	3.18	0.65	1.98	0.33	2.18	0.31	691.66	9.19	700.84	–
Std.	214.56	316.80	26.79	67.70	5.51	1.81	3.04	0.46	2.95	0.63	1.98	0.34	2.22	0.29	633.29	8.74	635.68	
V [%]	97	96	90	89	77	98	80	85	95	99	103	105	105	95	94	98	93	
W-36	181.30	264.69	26.41	60.56	4.72	1.17	2.85	0.39	1.57	0.30	1.02	0.14	0.91	0.13	541.70	4.46	546.16	Cu-concentrate
W-37	315.20	460.19	39.59	92.94	6.89	1.43	3.98	0.44	1.76	0.26	0.90	0.15	0.83	0.14	920.22	4.48	924.70	Fe-concentrate
W-39	887.70	1296.04	96.83	228.58	19.83	4.91	16.21	1.34	7.12	1.15	4.19	0.58	4.04	0.51	2550.10	18.93	2569.03	waste I
W-40	902.60	1317.79	77.75	235.03	17.70	4.66	3.40	0.78	5.50	1.08	3.52	0.54	3.84	0.55	2558.93	15.81	2574.74	waste II
W-44	1916.00	2796.78	189.15	504.94	34.56	8.70	0.31	0.99	7.31	1.46	4.71	0.71	5.21	0.65	5450.04	21.04	5471.08	waste out from tailing

MDL – detection limit; V – coefficient of variability; St.d. – standard deviation.
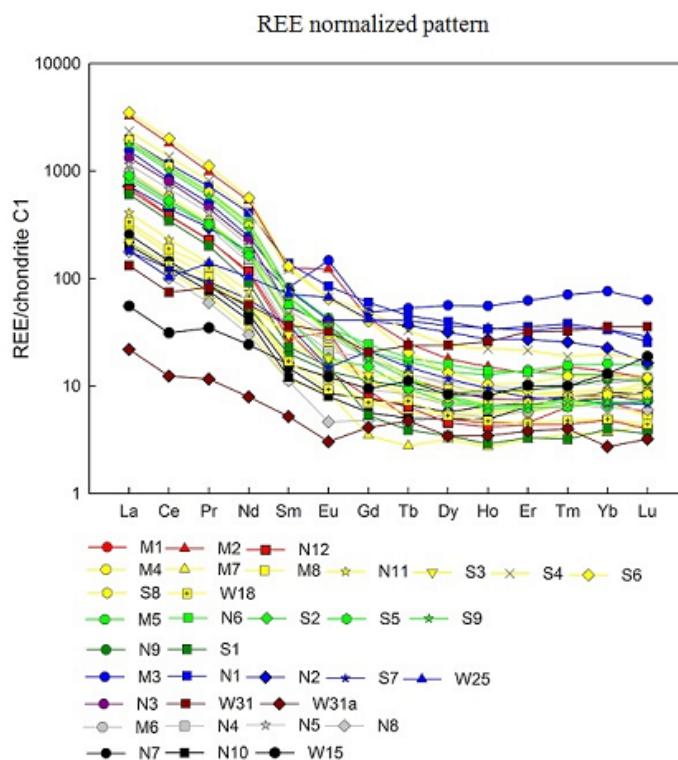
Fig. 4. REE metal content curves normalized to their contents in the C1chondrite; in the figure the red color marked for the samples collected from Cu-Fe ore hosted in amphibolite, the yellow for the samples from massive ore, the green for samples for Cu-Fe banded ore, most green for metamorphic amphibolite schists, blue – amphibolite, most red for skarn rock, grey for amphibolite hosting ore and black for Cu-ore hosted in quartz-amphibolite rocks

Rys. 4. Krzywe zawartości metali REE znormalizowane do ich zawartości w chondrycie C1, czerwone krzywe odnoszą się do próbek pobranych ze stref złożowych zlokalizowanych w amfibolitach, żółte reprezentują próbki z masywnych siarczków, zielone przedstawiają zawartości REE w rudach warstwowanych, ciemnozielone charakteryzują łupki amfibolowe z otoczenia złoża, a czarne krzywe charakteryzują rudy Cu zlokalizowane w skałach kwarcowo-amfibolowych

3.2. Deposit mineralogy

Based on an ore microscopy investigation of polished sections of ore samples, magnetite, pyrite, pyrrhotite, chalcopyrite, and sphalerite are the major minerals, while marcasite, tennantite, cubanite, mackinawite, arsenopyrite, galena, native-Bi, bismuthinite, electrum, native gold, molybdenite, uraninite and tellurides are the minor minerals. In the publication by Li and Zhou (Li and Zhou 2017), chevkinite, aeschynite, bastnäsite, epidote, titanite, zircon, F-apatite and columbite are also documented. Several styles of mineralization are recognized in the deposit:

- ◆ massive sulphide;
- ◆ massive magnetite;
- ◆ mixed oxide-sulphide;
- ◆ disseminated sulphide;
- ◆ vein hosted.

All styles are characterized by different ore mineral assemblages.

Based on the local distribution of the major minerals within the deposit, Gas'kov et al. (Gas'kov et al. 2012) divided the deposit into two zones. In the first zone, which is located in the central and eastern part of the deposit, pyrite, pyrrhotite and chalcopyrite are dominant. In the second zone, which is located in the western part of the deposit, chalcopyrite and magnetite are the principal ore minerals. In magnetite-dominant ores, chalcopyrite is very common. In the massive sulphide ore, chalcopyrite, cubanite, magnetite and pyrrhotite are the major minerals. Electrum is recognized in massive sulphide ores as 1–5 μm thick fine veinlets and as 1000-μm-long inclusions randomly distributed in pyrite and chalcopyrite. EDS measurements of the electrum indicate an average composition of 75.7 wt% of Au, and 24.3 wt% of Ag. Some Bi-S and Bi-Te minerals were also documented using the same methods. The most important Bi-S-Te mineral is tellurobismuthite containing 87.6 wt% Bi and 21.4 wt% Te. In addition to Cu sulphides, other important accompanying minerals are allanite and uraninite, which are the major carriers of REE, and U (Pieczonka et al. 2015, 2017, 2019).

3.3. Allanite in the deposit

Allanite is an abundant mineral in the deposit, usually it occurs either at low concentrations, 1–2 vol%, (Figures 5A–D), or very rarely as a major mineral (Figures 5 and 6). McLean (McLean 2001) reported up to 85% of allanite in hastingsite-biotite-quartz metasomatites and up to 10% in skarns, while the other scientists reported that the allanite content was 5–7 vol% in skarn and 5–30 vol% in the ore (Gas'kov et al. 2012; Li and Zhou 2018). Based on our data, in both the bulk chemical analyses (Table 1) and in the mineralogical study, the maximum content of allanite in the ore is 0.98 wt% (Table 1). This value was calculated by the equation as follows: the maximum REE content in the ore and host rock = 0.2463% (Table 1) multiplied by four (25% of ΣREE in the allanite itself). Allanites are typically present as subhedral grains intergrown with magnetite and amphibole (Figures 5A–D), with titanite, biotite and sulphides (Figures 5B) and commonly contain inclusions of these minerals. Allanites are also present as individual isometric grains and aggregates, up to 0.6 mm in size. In polished sections, grains of allanite minerals and their two populations can easily be identified in reflected light microscopy. The shadow observed on BSE pictures shows the second population with lower concentration of REE in comparison with that in the first population with lighter reflectivity (Figure 6). Both are usually present as intergrowths with only a small difference in reflectivity and smoothness. The outer rim is characterized
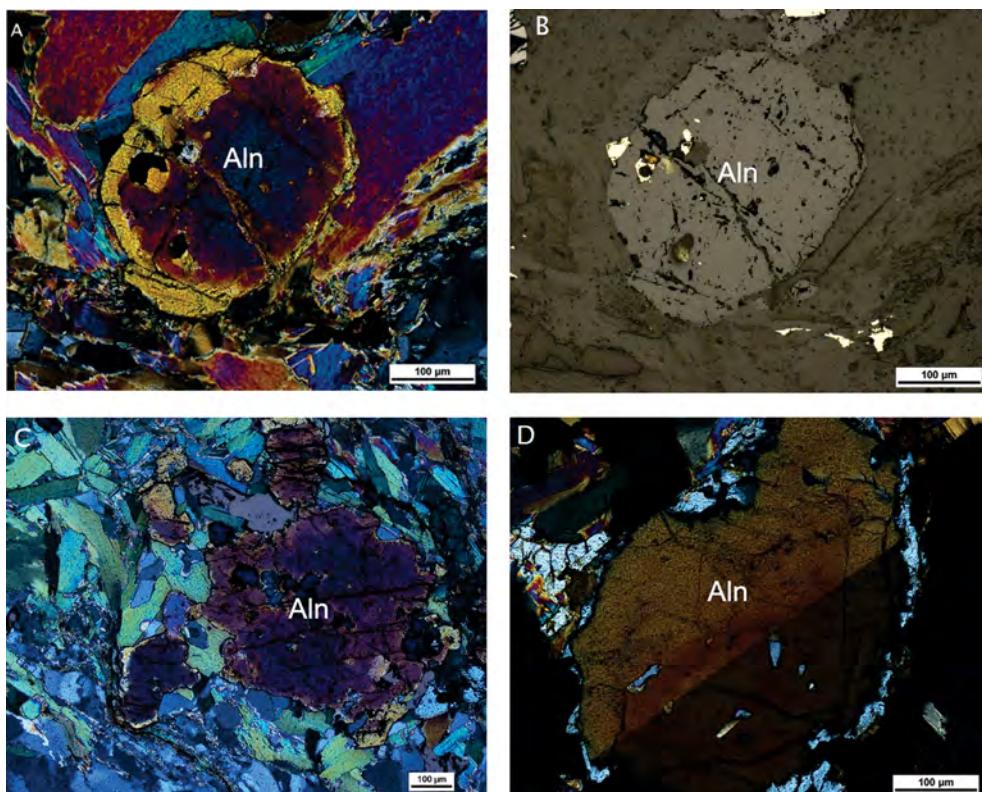
Fig. 5. Microphotographs of ore minerals from Sin Quyen deposit in transmitted (TL) and reflected light (RL)
A – Allanite crystal in pyroxene matrix (TL), B – Allanite grain with sulphide inclusions (RL),
C – altered allanite in pyroxene matrix (TL), D – allanite twins (TL)

Rys. 5. Mikrofotografie minerałów ze złoża Sin Quyen wykonane w świetle przechodzącym (TL) i odbitym (RL)
A – kryształ allanitu w matrycy piroksenowej (TL), B – Kryształ allanitu z siarczkami (białe, RL),
C – allanit przeobrażony w matrycy piroksenowej (TL), D – zbliźniaczony kryształ allanitu (TL)

with depleted hardness and lower reflectivity, close to the reflectivity of typical host minerals like feldspars and epidote. The contact between the two phases is distinct enough, which suggests epitaxial overgrowing is also clearly visible in the transmitted light of the optical microscope.

3.3.1. Chemical composition of allanites

WDS point measurement and WDS compositional maps (Figures 6A–E and 7Al, 7Ca, 7Ce, 7La, 7Nd, 7Fe) show a high degree of compositional variability in the allanite grains. The basic chemical compositions of allanites are summarized in Tables 2a, 2b, 3a and 3b. The first population (core) is characterized by a high ΣREE concentration of 20–27 wt%,
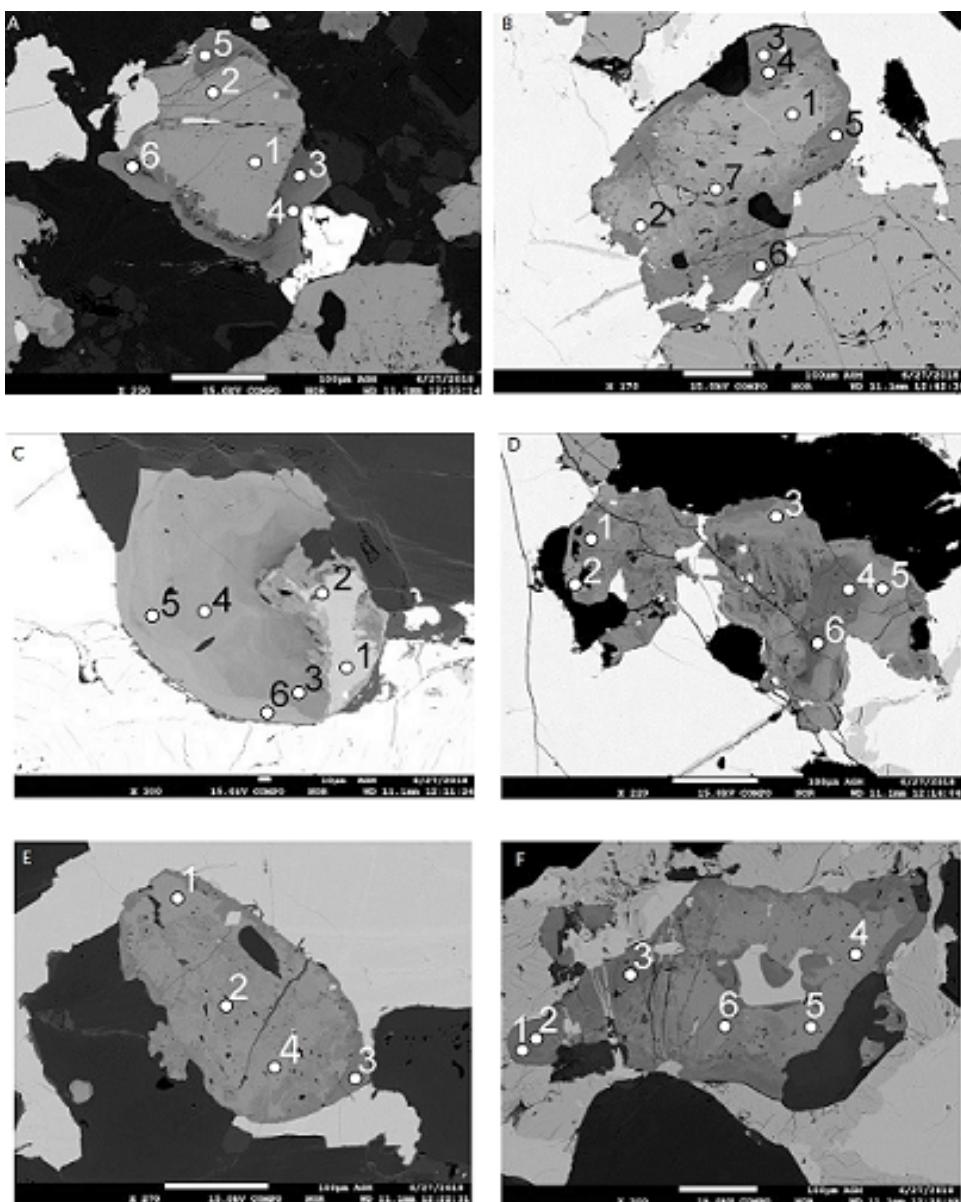
Fig. 6. Selected BSE-WDS (A–F) images of analyzed allanite grains. Gray shadows show changing
in chemical composition. Numbers on the pictures show positions of WDS measurements, sample N4
A – black are silicate, white-sulphides, B – white are sulphides, C – black are silicate, white-sulphides,
D – black are silicate, white-sulphides, E – black are silicate, white-sulphides,
F – black are silicate, white-sulphides

Rys. 6. Wybrane obrazy BSE-WDS (A–F) analizowanych allanitów. Szare odcienie pokazują zmiany w składzie
chemicznym. Numery na fotografiach pokazują miejsca wykonanych analiz, próbka N4
A–F – miejsca czarne są krzemianami; białe – siarczkami, miejsca szare z zaznaczonymi punktami
są allanitami
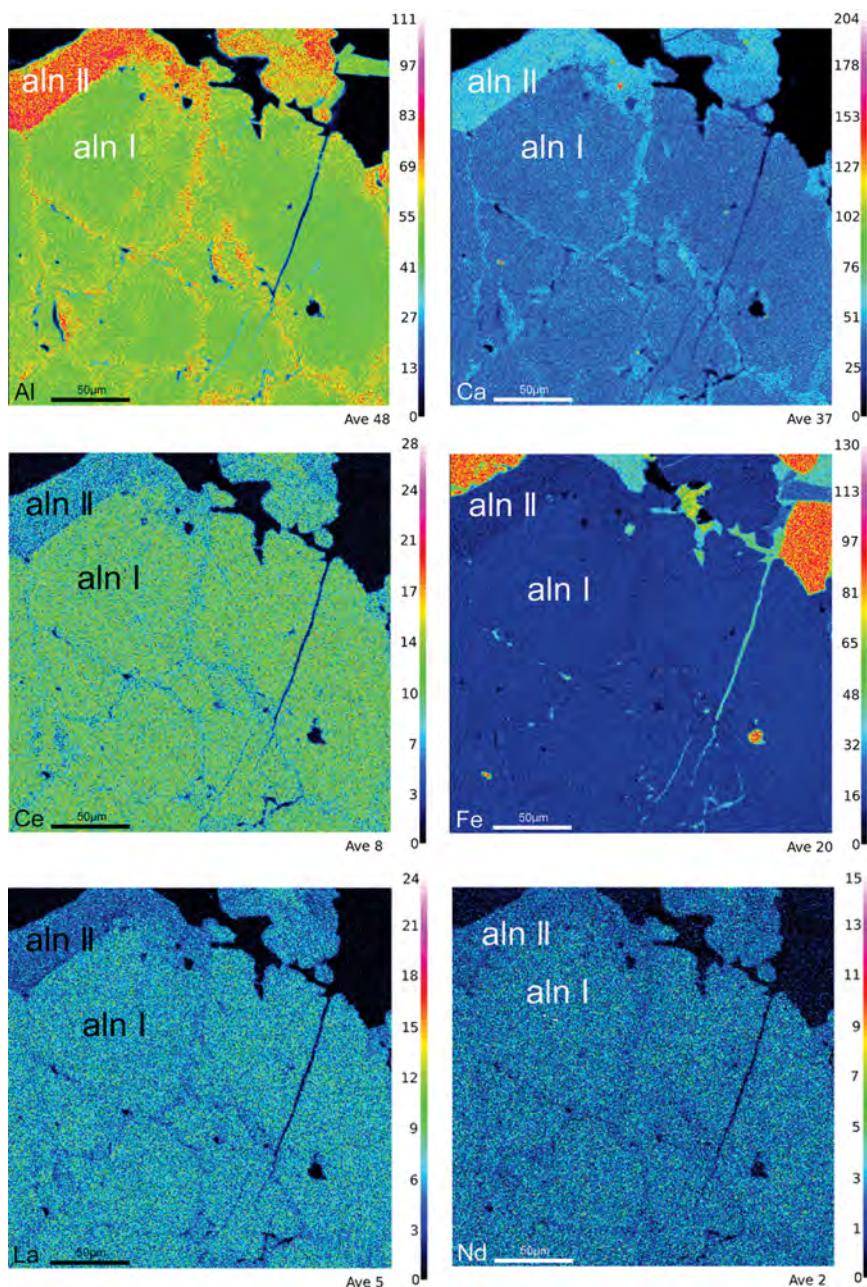
Fig. 7. WDS compositional maps of two allanite populations
Al – contour map of Al, Ca contour map of – Ca, Ce contour map of – Ce, Fe contour map of – Fe,
La contour map of – La, and Nd contour map of – Nd (revised from Hao et al. 2021)

Rys. 7. Mapy WDS rozmieszczenia pierwiastków w allanitach
Al – mapa rozmieszczenia glinu, Ca – mapa rozmieszczenia wapnia, Ce – mapa rozmieszenia ceru,
Fe – mapa rozmieszczenia żelaza, La – mapa rozmieszczenia lantanu, Nd – mapa rozmieszczenia neodymu

with an average of 24.04 wt%, and major constituents such as Si, Fe, Al and Ca (Table 2a). Cerium and lanthanum are the most abundant REEs. The second population (rim) is characterized by a lower ΣREE content, ranging from 14.1 to 19.9 wt%, with an average of 17.35 wt% (Table 2b), and by higher calcium values (Table 2a). The differences in allanite composition are also documented on BSE images (Figure 6A–F) and WDS compositional maps (Figure 7Al–7Fe) also show variations in allanite compositions. The outer rim is usually depleted in Ce, La and Nd (Figures 7Ce and 7La) and enriched in Ca and Al (Figure 7Ca and 7Al) (rf. Table 2a and 2b). Iron is higher in core allanites (rf. Table 2a and 2b). The slight differences in Fe concentration (around 3 wt%) is also shown on Figure 7Fe. However, grey tints showing Fe concentrations are not clearly visible and show only fine differences between two allanite populations (Figure 6). The sharp borders of the outer rim suggest two stages of allanite crystallization. This interpretation is supported by the variable chemical composition (Tables 2a, 2b and 3a, 3b) and textural development (Figure 6A–F). Similar observations were also noted by McLean (McLean 2001).

Pearson strong correlation and high variance (R^2) between CaO, Al_2O_3, ΣFeO vs $ΣREE_2O_3$ (Figure 8A, B and C) suggest the possible joined substitution of these elements by REE metals. The moderate variance (R^2) of SiO_2 vs $ΣREE_2O_3$ (Figure 8D) and the compa-
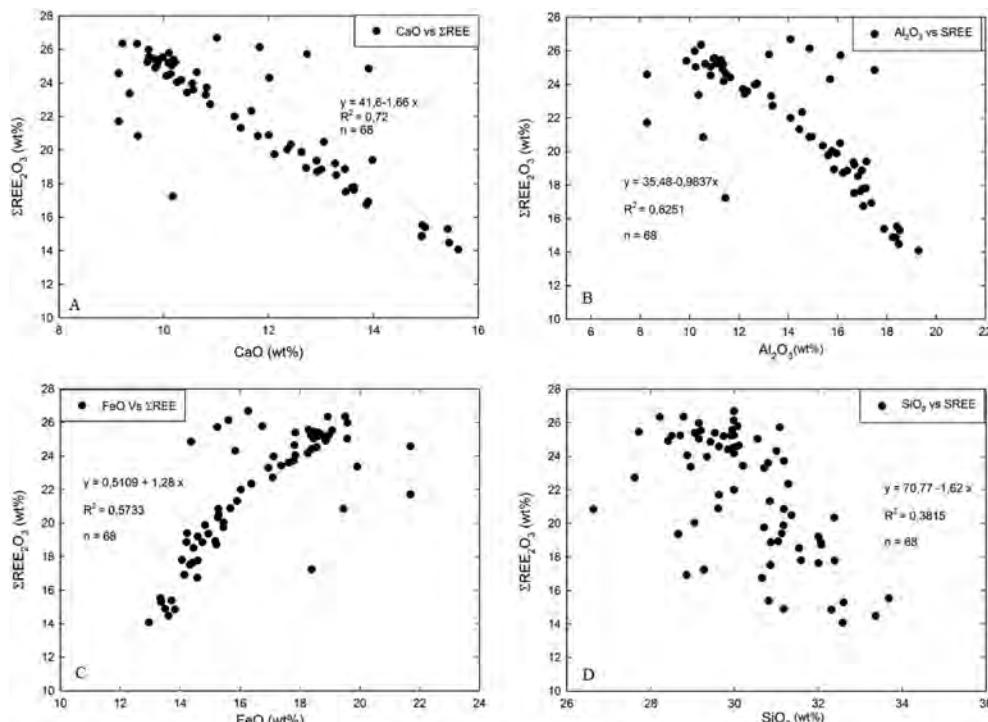
Fig. 8. Correlation between ΣREE and CaO, Al_2O_3, FeO, SiO_2 in allanite

Rys. 8. Korelacje między ΣREE i CaO, Al_2O_3, FeO, SiO_2 w allanitach

rability of the SiO_2 amounts in both allanite populations (Tables 2a and 2b) suggest that the changes in the silica composition are negligible.

3.3.2. Raman spectroscopy of allanites

Two optically and chemically different allanite populations were also examined using Raman spectroscopy (RS). First of all, the presence of the OH group can be indicated by broad bands in the region of 3300–3100 cm^{-1} (Shieh and Duffy 2002) in Raman spectra (Figures 9 and 10). This fact effectively explains the total of the elements analyzed by WDS to be below 100% (Tables 2a, 2b and 3a, 3b).

The second function of RS was confirmation that differences in the chemical composition of two allanites might have effects on both optical properties and RS spectra. The position of RS active bands at the region 1100–300 cm^{-1} recorded for Viet-5-001 crystal (first population) and Viet-5-002 crystal (second population) differ from each other (Figure 9 and 10); this is most probably due to the differences in the composition of these two phases. Lines 1052, 1045, 971, 909, and 871 cm^{-1} (Figures 9 and 10) stand as the main bands.
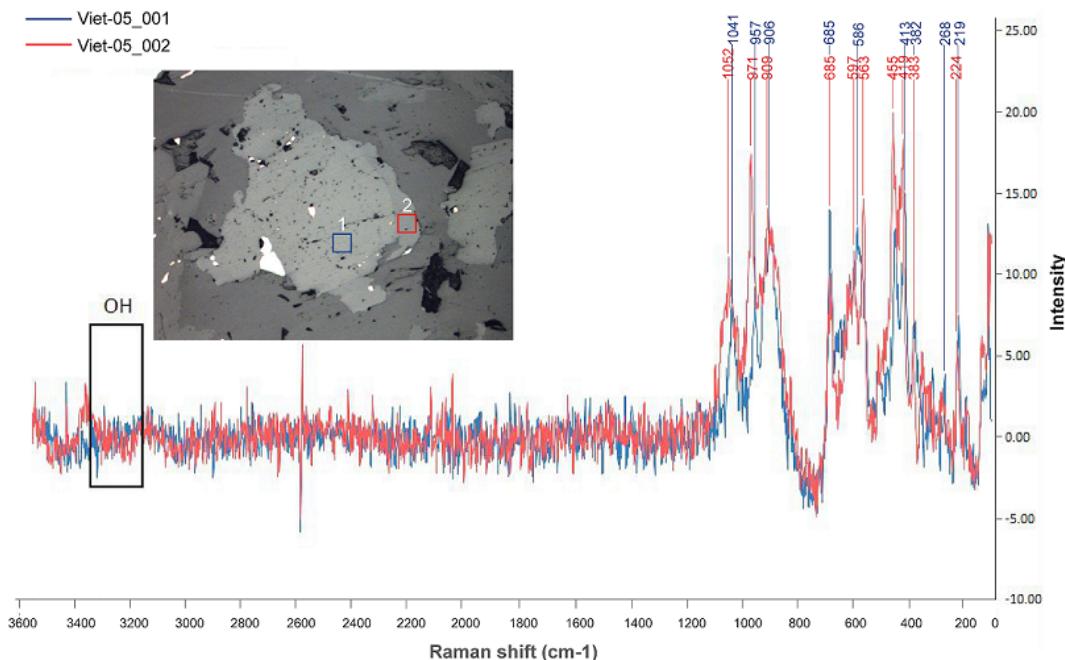
Fig. 9. Raman spectra of Viet-05_001 point (first population of allanite)
and Viet-05_002 point (second population)

Rys. 9. Widma Ramanowskie punktu Viet-05_001 (pierwsza populacja allanitu)
i punktu Viet-05_002 (druga populacja)
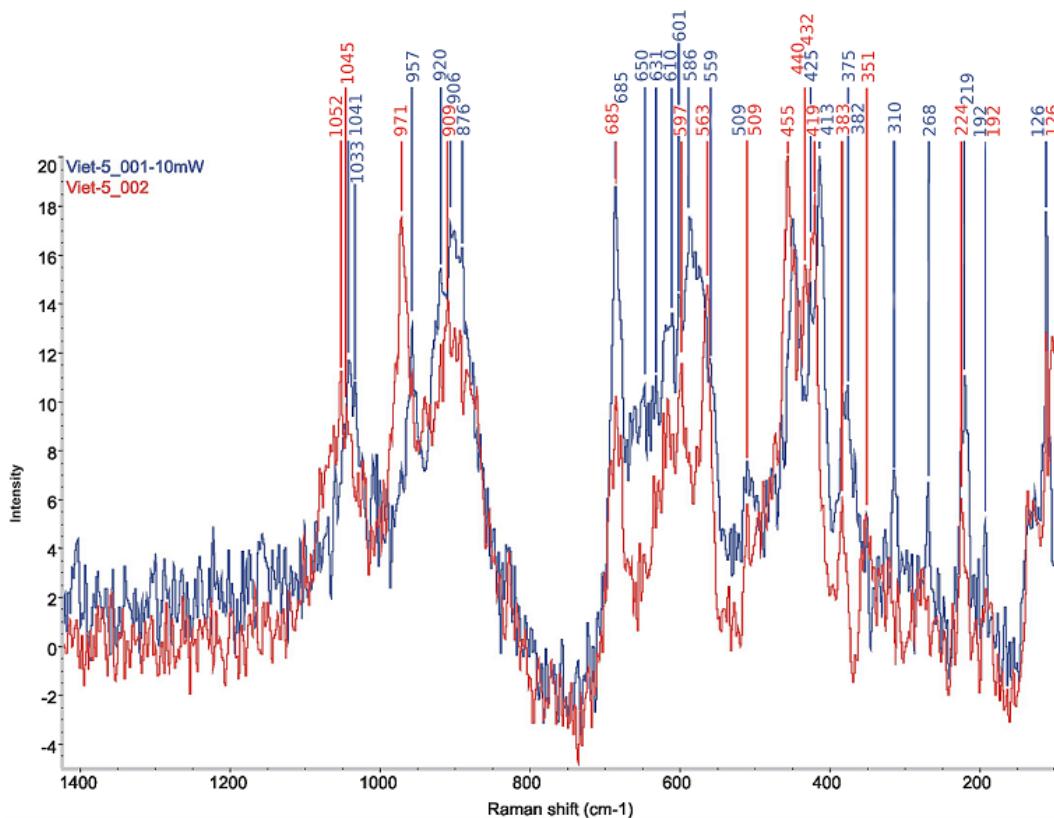
Fig. 10. Detail comparison of the Raman spectra two different allanites, sample, Viet-05_001 and Viet-05_002

Rys. 10. Porównanie szczegółowe widm Ramanowskich dwóch różnych odmian allanitów
Viet-05_001 i Viet-05_002

The detailed RS shifts are presented in Figure 10. The bands at 1041, 1033, 958, 920, 907 and 876 cm^{-1} are attributed to SiO_2 stretching vibrations, which is shifted towards higher wave numbers for Viet-5-002 crystal (Figure 10). The other shifts, e.g. 685, 650, 631, 610, 601, 586, 559, 509, 449, 439, 425, 413, 382, and 375 cm^{-1} of the spectral range 750–350 cm^{-1} are related to siloxane bending modes (Figure 9, Viet-5-001). At this range, the Raman banks of Viet-5-002 are also shifted towards higher wave numbers than for Viet-5-001 crystal (Figure 10). The Raman active bands appearing below 350 cm^{-1} regions, e.g. 310, 268, 219, 192, 126 cm^{-1} (Figures 9 and 10) are described as lattice vibrations (López and Frost 2015). The position of shifts presented on Figures 9 and 10 clearly indicate the significant changes in the allanite structure.

Table 2a. WDS composition of the first population of allanites with ΣREE$_2$O$_3$ higher than 20 wt%

Tabela 2a. Skład chemiczny pierwszej populacji allanitów o zawartości ΣREE$_2$O$_3$ większej od 20% wag.,
analiza WDS

No.	CaO	PbO	SiO$_2$	As$_2$O$_5$	Al$_2$O$_3$	FeO	MgO	MnO	TiO$_2$	Y$_2$O$_3$	ThO$_2$	ΣREE	Total	Comment
1	12.4	0.02	29.0	b.d.l.	15.8	15.4	0.18	0.05	0.14	0.00	0.03	20.04	93.1	AP465_fot13_p3
2	12.4	b.d.l.	32.4	b.d.l.	15.4	15.3	0.18	0.13	0.26	0.04	0.05	20.34	96.4	AP465_fot5_p4
3	13.1	0.02	31.4	0.03	16.1	15.3	0.14	0.10	0.34	0.01	0.02	20.49	95.7	AP464 (fig.7 6B)
4	9.51	0.01	26.6	0.15	10.6	19.5	0.47	0.09	0.26	0.06	0.01	20.85	93.3	AP464 (fig.7B)
5	12.0	0.01	29.6	0.02	15.0	15.7	0.19	0.12	0.34	0.05	0.02	20.86	93.9	AP464_fot1_p1
6	11.8	0.01	31.2	b.d.l.	14.7	15.3	0.17	0.10	0.26	0.06	0.06	20.89	94.7	AP465_fot4_p4
7	11.5	0.02	30.8	b.d.l.	14.5	15.9	0.22	0.14	0.30	b.d.l.	0.03	21.32	94.8	AP465 (fig.7E)
8	9.14	b.d.l.	29.6	0.14	8.27	21.7	0.31	0.11	0.32	0.11	0.03	21.71	96.0	AP465 (fig.7D)
9	11.4	0.01	30.0	0.06	14.1	16.0	0.20	0.15	0.34	0.06	0.05	22.00	94.3	AP465_fot4_p5
10	11.7	b.d.l.	31.3	b.d.l.	14.6	16.4	0.20	0.12	0.26	0.01	0.02	22.34	97.0	AP465 (fig.7B)
11	10.9	0.01	27.6	0.03	13.4	17.1	0.20	0.11	0.19	0.11	0.01	22.72	92.3	AP465 (fig.7F)
12	10.8	0.01	30.7	b.d.l.	13.3	17.0	0.23	0.09	0.28	0.06	0.02	23.30	95.9	AP465_fot13_p2
13	9.34	b.d.l.	29.0	0.11	10.4	19.9	0.26	0.13	0.31	0.04	0.02	23.37	95.6	AP465 (fig. 7D)
14	10.4	0.01	30.2	0.07	12.2	17.4	0.31	0.04	0.27	0.03	0.04	23.43	94.7	AP465 (fig.7E)
15	10.6	b.d.l.	30.8	0.04	12.3	17.6	0.24	0.11	0.28	0.01	0.10	23.60	95.6	AP465_fot4_p7
16	10.8	b.d.l.	31.2	0.10	12.2	17.8	0.36	0.12	0.51	0.03	0.05	23.72	96.8	AP465_fot5_p2
17	10.5	0.01	29.3	0.03	12.6	17.1	0.27	0.12	0.21	0.05	0.14	23.97	94.5	AP465_fot4_p6
18	10.3	b.d.l.	28.9	b.d.l.	12.7	17.8	0.12	0.05	0.24	0.12	b.d.l.	24.04	94.5	AP465 (fig.7C)
19	10.3	0.01	30.0	0.21	11.4	18.3	0.41	0.07	0.08	0.03	0.02	24.18	95.0	AP465_fot4_p2
20	12.0	0.01	31.0	0.02	15.7	15.8	0.18	0.14	0.31	b.d.l.	0.01	24.31	95.7	AP464 (fig.7B)
21	10.0	0.02	29.8	0.14	11.6	18.4	0.36	0.08	0.31	0.15	0.02	24.41	95.4	AP464 (fig.7A)
22	10.1	b.d.l.	30.0	0.20	10.9	18.6	0.46	0.05	0.14	0.04	0.09	24.53	95.0	AP465_fot4_p3
23	9.14	b.d.l.	29.6	0.14	8.27	21.7	0.31	0.11	0.32	0.04	0.02	24.58	96.0	AP465 (fig.7D)
24	10.6	0.02	30.1	0.18	11.5	17.8	0.59	0.04	0.30	0.04	0.02	24.64	95.8	AP465_fot14_p3
25	13.9	0.02	29.4	0.05	17.5	14.4	0.14	0.15	0.16	0.05	0.01	24.85	93.6	AP464 (fig.7A)

No.	CaO	PbO	SiO$_2$	As$_2$O$_5$	Al$_2$O$_3$	FeO	MgO	MnO	TiO$_2$	Y$_2$O$_3$	ThO$_2$	ΣREE	Total	Comment
26	9.84	b.d.l.	28.4	0.08	11.3	18.9	0.40	0.11	0.40	0.08	0.02	24.91	94.3	AP464 (fig.7A)
27	9.87	b.d.l.	29.2	0.17	10.8	18.5	0.51	0.05	0.18	0.07	0.05	25.04	94.5	AP465 (fig.7E)
28	10.2	0.03	30.6	0.10	10.2	19.6	0.39	0.17	0.64	0.07	0.09	25.04	97.2	AP465_fot5_p5
29	10.2	b.d.l.	28.7	0.28	11.2	18.4	0.57	0.05	0.22	0.03	0.03	25.20	94.8	AP465_fot14_p2
30	9.68	b.d.l.	30.0	0.19	11.1	18.7	0.54	0.02	0.21	0.08	0.02	25.22	95.7	AP465_fot13_p1
31	9.88	b.d.l.	28.5	0.15	10.6	18.5	0.55	0.05	0.18	0.08	0.08	25.24	93.8	AP465_fot4_p1
32	10.1	0.01	29.7	0.21	11.4	18.6	0.51	0.06	0.28	0.02	0.01	25.24	96.2	AP464_fot1_p4
33	9.88	b.d.l.	29.9	0.18	11.1	19.0	0.41	0.07	0.19	0.11	0.04	25.25	96.1	AP465 (fig.7F)
34	10.2	b.d.l.	29.5	0.27	11.3	18.6	0.50	0.05	0.27	b.d.l.	0.03	25.39	96.2	AP465_fot13_p4
35	9.90	b.d.l.	29.0	0.34	9.87	17.8	0.97	0.04	0.56	0.08	0.04	25.40	94.2	AP465_fot5_p1
36	9.81	b.d.l.	27.7	0.16	11.3	18.5	0.50	0.07	0.41	0.09	0.04	25.44	94.1	AP464_fot9_p5
37	10.0	0.02	29.2	0.18	11.0	19.1	0.42	0.09	0.24	0.05	0.03	25.5	95.8	AP465 (fig.7F)
38	9.72	b.d.l.	29.9	0.21	11.0	18.3	0.53	0.06	b.d.l.	0.03	0.05	25.57	95.4	AP465 (fig.7E)
39	12.7	b.d.l.	31.1	0.01	16.1	15.2	0.16	0.11	0.20	0.07	0.04	25.72	95.2	AP464_fot9_p3
40	10.1	b.d.l.	30.1	0.07	13.2	16.8	0.25	0.10	0.14	0.06	b.d.l.	25.79	96.5	AP465 (fig.7C)
41	9.71	b.d.l.	29.2	0.25	10.2	19.6	0.53	0.02	0.19	0.09	0.04	25.99	95.2	AP464 (fig.7B)
42	11.8	b.d.l.	30.0	0.04	14.9	15.6	0.13	0.12	0.09	0.20	0.01	26.14	94.9	AP465 (fig.7D)
43	9.49	0.02	28.2	0.18	10.5	18.9	0.55	0.08	0.48	0.04	0.03	26.34	94.9	AP464_fot1_p3
44	9.21	b.d.l.	28.8	0.15	10.5	19.5	0.32	0.14	0.13	0.00	0.04	26.36	95.5	AP465 (fig.7D)
45	11.0	0.02	30.0	b.d.l.	14.1	16.3	0.15	0.18	0.13	0.10	0.02	26.69	95.4	AP465 (fig.7D)
min.	9.14	0.00	26.6	0.00	8.27	14.4	0.12	0.02	0.00	0.00	0.00	20.04	92.3	
max.	13.9	0.03	32.4	0.34	17.5	21.7	0.97	0.18	0.64	0.20	0.14	26.69	97.2	
Av.	10.62	0.01	29.7	0.11	12.37	17.72	0.35	0.09	0.26	0.06	0.04	24.04	95.14	n = 45
St.d.	1.12	0.01	1.11	0.09	2.18	1.70	0.18	0.04	0.12	0.04	0.03	1.84	1.05	
V (%)	10.6	12.89	3.7	83.4	17.7	9.6	50.6	42.9	46.8	74.1	77.8	7.7	1.1	

Sought but not detected: U, F, S and Sc; b.d.l. – below detection limit; St.d. – standard deviation; Av – average content; V – coefficient of variability.

Table 2b.   WDS composition of second population of allanites with ΣREE_2O_3 lower than 20 wt%

Tabela 2b.   Skład chemiczny drugiej populacji allanitów o zawartości ΣREE_2O_3 mniejszej niż 20 % wag.,
analiza WDS

No.	CaO	PbO	SiO$_2$	As$_2$O$_5$	Al$_2$O$_3$	FeO	MgO	MnO	TiO$_2$	Y$_2$O$_3$	ThO$_2$	ΣREE_2O_3	Total	Comment
1	15.618	0.004	32.576	b.d.l.	19.291	12.959	0.082	0.092	0.117	0.100	0.014	14.08	94.976	AP465_fot5_p3
2	15.444	0.020	33.370	b.d.l.	18.490	13.611	0.066	0.149	0.150	0.207	0.003	14.48	95.995	AP464 (fig.7A)
3	14.918	0.035	32.312	0.052	18.360	13.825	0.090	0.106	0.139	0.173	0.020	14.85	95.083	AP464_fot9_p4
4	14.920	0.024	31.174	b.d.l.	18.242	13.497	0.076	0.149	0.119	0.278	0.034	14.89	93.414	AP465_fot7_p3
5	14.933	0.020	33.679	b.d.l.	18.410	13.340	0.095	0.145	0.087	0.092	b.d.l.	15.53	96.329	AP465_fot1_p4
6	14.987	0.003	30.815	b.d.l.	17.889	13.711	0.073	0.150	0.178	0.148	0.048	15.38	93.283	AP465_fot14_p1
7	14.933	0.020	33.679	b.d.l.	18.410	13.340	0.095	0.145	0.087	0.092	b.d.l.	15.53	96.329	AP465_fot1_p4
8	13.868	b.d.l.	30.655	0.003	17.040	14.569	0.129	0.171	0.224	0.130	0.020	16.74	93.388	AP465 (fig.7F)
9	13.898	b.d.l.	28.854	0.098	17.377	14.147	0.124	0.149	0.154	0.077	0.027	16.93	92.015	AP464 (fig.7A)
10	10.164	0.011	29.268	0.160	11.447	18.392	0.394	0.071	0.523	0.087	0.011	17.24	95.222	AP464_fot9_p1
11	13.469	b.d.l.	30.855	0.035	16.675	14.327	0.154	0.139	0.185	0.093	0.004	17.51	93.284	AP465_fot1_p3
12	13.626	0.019	31.997	b.d.l.	16.928	14.406	0.124	0.164	0.203	0.068	0.041	17.64	95.214	AP465_fot10_p3
13	13.588	0.020	32.383	b.d.l.	17.018	14.585	0.142	0.112	0.200	0.039	0.045	17.77	96.007	AP465_fot12_p7
14	13.629	0.017	31.588	b.d.l.	17.153	14.062	0.123	0.133	0.117	0.168	0.019	17.80	94.874	AP465 (fig.7C)
15	12.924	0.024	32.067	0.066	16.225	15.206	0.146	0.190	0.246	0.160	0.018	18.72	96.089	AP465_fot10_p2
16	13.005	b.d.l.	32.056	0.078	16.387	14.741	0.138	0.071	0.144	0.089	b.d.l.	18.86	95.464	AP465 (fig.7C)
17	13.454	0.020	30.863	b.d.l.	16.984	14.219	0.119	0.142	0.193	0.219	0.010	18.86	94.650	AP465_fot10_p1
18	12.712	0.005	31.038	b.d.l.	15.853	15.173	0.146	0.149	0.269	0.048	0.036	18.93	95.200	AP464_fot10_p4
19	13.269	b.d.l.	31.997	0.006	16.679	14.586	0.111	0.143	0.198	0.186	b.d.l.	19.21	96.245	AP465 (fig.7C)
20	12.912	0.019	28.655	0.019	16.646	14.941	0.168	0.175	0.119	0.092	0.052	19.37	93.104	AP464_fot1_p2
21	13.979	0.008	31.127	b.d.l.	17.172	14.228	0.158	0.155	0.166	b.d.l.	0.009	19.39	94.366	AP464_fot9_p2
22	12.110	0.036	30.701	0.010	15.613	15.445	0.182	0.139	0.393	0.101	0.038	19.75	95.558	AP464_fot10_p3
23	12.626	b.d.l.	31.165	b.d.l.	15.956	14.831	0.165	0.113	0.151	0.119	0.023	19.89	94.875	AP465_fot12_p1
min.	10.164	0.000	28.655	0.000	11.447	12.959	0.052	0.071	0.087	0.000	0.000	14.080	92.015	
max.	15.618	0.036	33.679	0.160	19.291	18.392	0.394	0.190	0.523	0.278	0.052	19.89	96.329	
Av.	13.716	0.014	31.382	0.023	16.972	14.442	0.133	0.137	0.191	0.121	0.021	17.35	94.795	n = 23
St.d.	1.264	0.012	1.282	0.042	1.546	1.081	0.067	0.031	0.097	0.064	0.017	1.865	1.181	
V (%)	9.2	86.7	4.1	180.5	9.1	7.5	50.5	22.2	50.9	53.0	80.1	10.7	1.2	

Sought but not detected: U, S and Sc; b.d.l. – below detection limit; Av – average content; St.d. – standard deviation; V – coefficient of variability.

Table 3a.   WDS concentrations of REE in the first population of the allanite in wt%

Tabela 3a.   Koncentracje REE w allanitach pierwszej populacji, analiza WDS w % wag.

No.	La_2O_3	Ce_2O_3	Pr_2O_3	Nd_2O_3	Sm_2O_3	Eu_2O_3	$\Sigma LREE$	Gd_2O_3	Tb_2O_3	Dy_2O_3	Ho_2O_3	Yb_2O_3	Lu_2O_3	$\Sigma HREE$	ΣREE	$\Sigma LREE/$ $/\Sigma HREE$
1	5.89	9.89	1.04	2.84	0.21	b.d.l.	19.86	0.03	0.09	0.03	0.02	0.01	b.d.l.	0.173	20.04	115
2	6.77	10.22	0.99	2.07	0.10	b.d.l.	20.16	0.09	0.04	b.d.l.	b.d.l.	0.02	0.02	0.178	20.34	113
3	6.86	10.05	0.86	2.15	0.18	0.06	20.16	0.17	0.07	0.05	b.d.l.	b.d.l.	0.04	0.330	20.49	61
4	6.94	10.23	0.89	2.36	0.20	0.04	20.66	b.d.l.	0.09	0.06	0.04	b.d.l.	b.d.l.	0.190	20.85	109
5	6.02	10.21	1.10	3.06	0.27	0.02	20.69	b.d.l.	0.07	b.d.l.	0.10	b.d.l.	b.d.l.	0.169	20.86	122
6	6.94	10.79	0.90	2.06	0.08	0.02	20.78	0.03	0.08	b.d.l.	b.d.l.	b.d.l.	b.d.l.	0.108	20.89	192
7	7.61	10.64	0.81	1.96	0.14	0.03	21.18	b.d.l.	0.05	0.05	0.02	0.01	b.d.l.	0.135	21.32	157
8	4.43	10.55	1.34	4.56	0.50	0.06	21.44	b.d.l.	0.05	0.02	0.06	0.09	0.04	0.266	21.71	81
9	6.12	10.84	1.16	3.34	0.24	0.05	21.75	0.16	0.05	0.04	b.d.l.	b.d.l.	b.d.l.	0.245	22.00	89
10	6.78	10.82	1.08	3.17	0.25	0.04	22.14	b.d.l.	0.04	0.07	0.09	b.d.l.	b.d.l.	0.202	22.34	110
11	7.71	11.26	0.96	2.44	0.14	0.01	22.53	0.13	0.03	b.d.l.	b.d.l.	0.02	b.d.l.	0.197	22.72	114
12	7.65	11.94	1.06	2.38	0.15	b.d.l.	23.19	b.d.l.	0.10	b.d.l.	b.d.l.	0.01	b.d.l.	0.107	23.30	217
13	5.25	11.77	1.30	4.41	0.35	0.06	23.14	b.d.l.	0.07	0.04	0.04	0.09	b.d.l.	0.232	23.37	100
14	8.07	11.79	1.00	2.30	0.17	0.01	23.33	b.d.l.	0.02	0.02	0.05	b.d.l.	b.d.l.	0.099	23.43	236
15	7.91	11.64	1.15	2.44	0.19	b.d.l.	23.33	0.09	0.09	0.02	b.d.l.	0.03	0.04	0.267	23.60	87
16	8.39	11.84	0.96	2.18	0.13	0.01	23.51	b.d.l.	0.10	0.04	0.03	0.04	b.d.l.	0.211	23.72	111
17	8.11	12.19	0.98	2.33	0.13	0.03	23.77	0.12	0.02	0.03	b.d.l.	0.02	b.d.l.	0.203	23.97	117
18	8.18	10.28	1.13	3.60	0.56	0.10	23.86	0.10	0.05	0.03	b.d.l.	b.d.l.	b.d.l.	0.186	24.04	128
19	8.64	12.30	0.96	2.05	0.07	0.02	24.05	0.05	0.06	0.03	b.d.l.	b.d.l.	b.d.l.	0.131	24.18	184
20	8.46	12.09	1.03	2.38	0.13	b.d.l.	24.09	0.07	0.11	0.01	b.d.l.	b.d.l.	0.04	0.223	24.31	108
21	7.85	12.73	1.16	2.46	0.11	0.01	24.31	b.d.l.	0.06	b.d.l.	0.02	0.01	b.d.l.	0.099	24.41	246
22	8.58	12.07	1.11	2.43	0.13	b.d.l.	24.33	0.07	0.09	0.02	b.d.l.	b.d.l.	0.02	0.194	24.53	125
23	6.05	12.77	1.28	3.96	0.27	0.05	24.38	0.09	0.04	0.05	b.d.l.	0.02	b.d.l.	0.207	24.58	118
24	8.62	12.20	1.04	2.55	0.08	0.04	24.52	0.03	0.07	b.d.l.	b.d.l.	b.d.l.	0.02	0.118	24.64	208
25	8.36	12.37	1.15	2.52	0.16	0.01	24.57	0.12	0.04	0.06	0.05	0.01	b.d.l.	0.280	24.85	88

Table 3a.　cont.

Tabela 3a.　cd.

No.	La_2O_3	Ce_2O_3	Pr_2O_3	Nd_2O_3	Sm_2O_3	Eu_2O_3	$\Sigma LREE$	Gd_2O_3	Tb_2O_3	Dy_2O_3	Ho_2O_3	Yb_2O_3	Lu_2O_3	$\Sigma HREE$	ΣREE	$\Sigma LREE/ \Sigma HREE$
26	8.65	12.71	1.07	2.23	0.05	0.02	24.73	0.01	0.09	b.d.l.	0.05	0.03	b.d.l.	0.177	24.91	140
27	8.53	12.86	1.04	2.29	0.11	0.05	24.88	0.05	0.04	0.04	0.01	0.02	b.d.l.	0.159	25.04	156
28	8.96	12.40	1.10	2.30	0.13	0.01	24.90	0.05	0.07	b.d.l.	b.d.l.	0.02	b.d.l.	0.133	25.04	187
29	9.02	12.37	0.94	2.55	0.11	0.04	25.05	0.08	0.05	b.d.l.	b.d.l.	0.02	b.d.l.	0.159	25.20	158
30	8.81	12.50	1.06	2.46	0.14	0.03	24.99	0.03	0.12	b.d.l.	0.04	0.03	b.d.l.	0.229	25.22	109
31	8.96	12.67	1.04	2.22	0.17	0.02	25.08	0.09	0.08	b.d.l.	b.d.l.	b.d.l.	b.d.l.	0.164	25.24	153
32	8.76	12.52	1.05	2.39	0.10	0.01	25.06	0.06	0.06	b.d.l.	0.01	b.d.l.	0.05	0.182	25.24	138
33	8.79	12.78	1.09	2.30	0.11	0.01	25.07	0.11	0.02	0.02	0.01	0.03	b.d.l.	0.184	25.25	136
34	8.56	12.91	1.13	2.49	0.14	0.01	25.25	b.d.l.	0.07	0.02	0.05	b.d.l.	b.d.l.	0.139	25.39	182
35	9.08	1255	1.02	2.47	0.14	b.d.l.	25.27	0.01	0.04	0.01	0.07	0.01	b.d.l.	0.131	25.40	193
36	8.78	12.98	1.11	2.31	0.10	b.d.l.	25.28	0.01	0.11	0.02	b.d.l.	b.d.l.	0.02	0.163	25.44	155
37	9.15	12.96	1.02	2.34	0.17	b.d.l.	25.37	0.06	0.05	0.03	b.d.l.	0.02	b.d.l.	0.156	25.53	163
38	9.15	12.98	0.98	2.29	0.01	0.02	25.42	b.d.l.	0.01	0.01	0.13	0.01	b.d.l.	0.145	25.57	175
39	8.88	12.81	1.21	2.44	0.13	0.01	25.48	0.08	0.09	0.07	0.01	b.d.l.	b.d.l.	0.243	25.72	105
40	6.80	13.35	1.36	3.73	0.25	0.03	25.53	b.d.l.	0.13	b.d.l.	0.06	0.02	0.05	0.257	25.79	99
41	9.16	12.96	1.08	2.53	0.09	0.01	25.83	0.06	0.05	0.02	b.d.l.	0.03	b.d.l.	0.157	25.99	165
42	6.90	13.61	1.39	3.80	0.17	0.02	25.88	b.d.l.	0.08	0.05	0.12	0.02	b.d.l.	0.253	26.14	102
43	8.97	13.45	1.08	2.54	0.13	0.02	26.20	0.03	0.07	0.04	b.d.l.	b.d.l.	b.d.l.	0.148	26.34	177
44	7.97	13.40	1.29	3.27	0.16	0.03	26.11	b.d.l.	0.04	0.01	0.07	0.13	0.02	0.256	26.36	102
45	7.49	13.84	1.39	3.56	0.15	0.06	26.50	b.d.l.	0.13	0.01	b.d.l.	0.04	0.02	0.192	26.69	138
min.	4.43	9.89	0.81	1.96	0.01	0.01	19.86	0.01	0.01	0.01	0.01	0.01	0.02	0.10	20.04	61.00
max.	9.16	13.80	1.39	4.56	0.56	0.10	26.50	0.17	0.13	0.07	0.13	0.13	0.05	0.33	26.69	246.00
Av.	7.83	12.04	1.09	2.69	0.17	0.03	23.82	0.07	0.07	0.03	0.05	0.03	0.02	0.19	24.01	137.73
St.d.	1.16	1.10	0.14	0.64	0.10	0.02	1.85	0.04	0.03	0.02	0.03	0.03	0.01	0.05	1.85	43.84
V (%)	14.86	9.13	12.67	23.98	61.54	70.34	7.79	60.29	44.99	55.22	69.02	95.60	65.79	28.70	7.70	31.83

Notes: Sought but not detected: U, S and Sc; b.d.l. – below detection limit; Av – average content; St.d.– standard deviation; V – coefficient of variability.

Table 3b. WDS concentrations [wt%] of rare earth elements in second population of the allanite

Tabela 3b. Koncentracje REE w allanitach drugiej populacji, analiza WDS w % wag.

No.	La_2O_3	Ce_2O_3	Pr_2O_3	Nd_2O_3	Sm_2O_3	Eu_2O_3	$\Sigma LREE$	Gd_2O_3	Tb_2O_3	Dy_2O_3	Ho_2O_3	Yb_2O_3	Lu_2O_3	$\Sigma HREE$	ΣREE	$\Sigma LREE/ \Sigma HREE$
1	4.43	6.95	0.56	1.66	0.16	0.04	13.8	0.11	0.04	0.08	b.d.l.	b.d.l.	0.06	0.280	14.08	49
2	4.98	6.95	0.67	1.56	0.11	0.01	14.3	0.04	0.08	0.06	0.01	b.d.l.	b.d.l.	0.197	14.48	72
3	4.58	7.26	0.70	1.90	0.23	0.05	14.72	0.04	0.04	b.d.l.	0.04	b.d.l.	0.01	0.126	14.85	117
4	3.81	7.05	0.77	2.62	0.32	0.02	14.6	0.13	0.04	0.09	0.03	b.d.l.	0.01	0.296	14.89	49
5	5.15	7.49	0.68	1.65	0.13	0.02	15.12	0.08	0.03	0.02	b.d.l.	0.04	0.01	0.172	15.30	88
6	5.04	7.61	0.75	1.57	0.12	b.d.l.	15.10	0.11	0.04	0.08	b.d.l.	b.d.l.	0.06	0.280	15.38	54
7	4.74	7.81	0.74	1.80	0.24	0.03	15.40	0.02	0.07	0.01	0.06	0.01	b.d.l.	0.162	15.53	95
8	4.30	7.95	0.87	2.93	0.32	0.07	16.43	0.12	0.07	0.07	0.02	b.d.l.	0.04	0.306	16.74	54
9	5.34	8.41	0.75	2.00	0.22	0.05	16.76	0.08	0.06	0.01	0.01	b.d.l.	0.01	0.164	16.93	102
10	5.76	8.54	0.68	1.96	0.12	0.05	17.11	0.02	0.07	b.d.l.	b.d.l.	0.03	0.01	0.129	17.24	133
11	5.45	8.58	0.89	2.04	0.22	0.01	17.19	0.13	0.07	b.d.l.	b.d.l.	0.03	0.08	0.316	17.51	54
12	4.86	8.62	0.85	2.75	0.27	0.01	17.37	0.13	0.05	0.08	b.d.l.	0.01	b.d.l.	0.268	17.64	65
13	4.84	8.56	0.97	2.93	0.29	0.07	17.66	0.02	0.05	b.d.l.	b.d.l.	0.01	0.03	0.110	17.77	161
14	3.98	8.41	1.09	3.46	0.41	0.03	17.38	0.28	0.08	b.d.l.	0.04	0.02	b.d.l.	0.420	17.80	41
15	6.13	9.57	b.d.l.	2.43	0.20	0.16	18.49	0.13	0.04	0.04	0.02	b.d.l.	b.d.l.	0.233	18.72	79
16	4.46	9.45	0.98	3.24	0.34	0.05	18.52	0.15	0.07	0.10	b.d.l.	0.02	b.d.l.	0.338	18.86	55
17	5.27	9.05	0.95	2.63	0.34	0.05	18.29	0.20	0.11	0.11	0.02	0.11	0.03	0.575	18.86	32
18	6.19	9.67	0.83	1.97	0.12	0.01	18.80	0.04	0.07	b.d.l.	b.d.l.	b.d.l.	0.02	0.136	18.93	138
19	5.06	9.11	1.03	3.17	0.34	0.02	18.73	0.24	0.05	0.09	b.d.l.	0.04	0.05	0.475	19.21	39
20	6.73	9.55	0.84	1.96	0.12	0.01	19.22	0.01	0.04	0.06	b.d.l.	0.05	b.d.l.	0.145	19.37	133
21	6.58	9.30	0.95	2.16	0.21	0.02	19.21	0.11	0.04	0.03	b.d.l.	0.01	b.d.l.	0.182	19.39	106
22	6.52	9.96	0.95	1.99	0.18	0.01	19.60	b.d.l.	0.08	0.02	0.06	b.d.l.	b.d.l.	0.155	19.75	126
23	5.46	9.73	1.11	3.04	0.27	0.07	19.67	0.08	0.04	0.04	0.04	b.d.l.	0.02	0.214	19.89	92
min.	3.81	6.95	0.56	1.56	0.11	0.01	13.8	0.01	0.03	0.01	0.01	0.01	0.01	0.110	14.08	32
max.	6.73	9.96	1.11	3.46	0.41	0.16	19.67	0.28	0.11	0.11	0.06	0.11	0.08	0.575	19.89	161
Av.	5.2	8.5	0.8	2.3	0.2	0.04	17.2	0.1	0.1	0.1	0.0	0.0	0.0	0.2	17.4	84.9
St.d.	0.8	1.0	0.1	0.6	0.1	0.0	1.8	0.1	0.0	0.0	0.0	0.0	0.0	0.1	1.8	37.7
V (%)	15.4	11.2	17.0	24.9	37.7	84.6	10.6	69.2	33.7	57.1	60.3	89.1	76.6	48.7	10.6	44.4

Notes: Sought but no detected: Er. Tm; b.d.l. – below detection limit; Av. – average content; St.d. – standard deviation, V – coefficient of variability.

4. Discussion

4.1. Allanite populations

Allanite are the most common REE minerals occurring in the deposit and surrounding rocks (Ishihara et al. 2011; Gas'kov et al. 2012). In some polished sections, the concentration of allanite reaches 1 to 5% by volume (e.g. sample no. M5, S4, S9 – massive ores). REE is also present in monazite, chevkinite, aeschynite, bastnäsite, apatite, pyrochlore (Gas'kov et al. 2012; Li et al. 2018), titanites and uraninite (Pieczonka et al. 2019). The average content of ΣREE in uraninites is relatively high (4.58 wt%) (Pieczonka et al. 2019). However, these minerals are rarely observed in the ores, and their influence on the total volume of REE in the deposit is negligible. In the massive sulphide, allanite concentrations reach up to several vol%, and epidote reaches up to 5 vol% (Ishihara et al. 2011). However, the bulk chemical data (Table 1) show that the average content of ΣREE is low – 701 ppm. This value roughly corresponds to 0.28% of allanite by volume. According to Gas'kov et al. (Gas'kov et al. 2012), epidote is the dominant mineral in some sections and can also contain certain amounts of REE.

The two different allanite populations have also been documented through the routine microscopic observation of ore. The polished surface of low REE allanite (second population) is smoother, and this mineral is also characterized by lower reflectivity (Ngo et al. 2020). Differences in these allanite populations are clearly observed in the amounts of Al_2O_3, CaO and total iron oxide (Tables 2a and 2b). The average concentration of CaO and Al_2O_3 in first population is 13.9 wt% and 17.5 wt%, respectively, while in the second, these oxides are 15.6 wt% and 19.3 wt%, respectively (Tables 2a and 2b). The amounts of SiO_2 in both populations are comparable. The total Fe oxides in the first population is 21.7 wt% and in the second, this value is 18.4 wt% in average. These values classify the investigated minerals as ferriallanite (Armbruster et al. 2006; http://webmineral.com/data/Ferriallanite-(Ce). shtml#.X8UMq2hKhaQ). The average concentration of La and Ce in the first population are 9.16 wt% and 13.8 wt%, while in the second, it is 6.73 wt% and 9.96 wt%, respectively (Tables 3a and 3b). Therefore, the cerium and lanthanum are dominant in allanite and the ratio Ce/La in both allanite populations varies from 1.48 to 2.32 so the considered allanite can be named as Ce-La-ferriallanite. The presence of two different allanite compositions is also visible on quantitative WDS compositional maps (Figure 7 Al–Fe). The allanite outer rim is younger. Different gray tints show the mosaic textures of allanite crystals. The rim surrounding some allanite grains can be interpreted as an epitaxial allanite overgrowth from solutions with decreasing REE content during the final crystallization phase. The chemical variability could be related to couple substitution of REE^{3+} and Fe^{2+} by Ca^{2+} and Fe^{3+} ($REE^{3+} + Fe^{2+} \leftrightarrow Ca^{2+} + Fe^{3+}$) (Ishihara et al. 2011). The relationship between the total REE and Ca + (Fe^{3+}) + Al expressed in apfu (Armbruster et al. 2006) for the WDS analyzed points of the two allanite populations is presented in Figure 11, which clearly indicates the
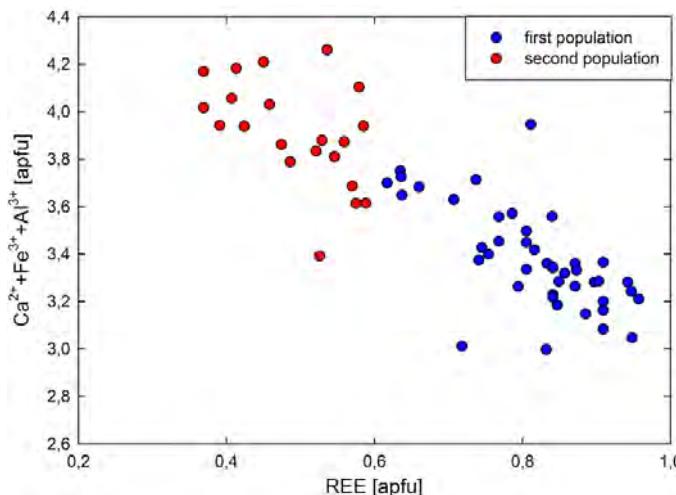
Fig. 11. ΣREE (apfu) versus Ca + Fe^{3+} + Al (apfu) based on selected WDS point analyses

Rys. 11. ΣREE (apfu) vs Ca + Fe^{3+} + Al (apfu) na podstawie wybranych punktów analizy WDS

difference between them. Statistical parameters calculated separately for the two populations of allanites show low values of standard deviation (Std.) and the coefficient of variability (V) for all the major elements (Tables 2a, 2b, 3a and 3b).

Higher variability of both the V and Std. parameters are recorded for most of the minor constituents (Tables 2a, 2b, 3a and 3b). The correlations calculated for the basic elements in the allanites show good Pearson correlation between CaO, Al_2O_3, FeO and low correlation of SiO_2 vs ΣREE_2O_3 (Figure 8A–D). The negative correlation of CaO and Al_2O_3 vs ΣREE might suggest the replacement of both cations by REE during hydrothermal alteration and recrystallization. A positive correlation was only noted for FeO – REE_2O_3, R = 0.76, indicating that Fe could be accompanied by REE. Variability in the chemical composition of the allanites can also suggest substitutions expressed as: $REE^{3+} + Fe^{2+} = Ca^{2+} + Fe^{3+}$ and $REE^{3+} + Fe^{2+} = Ca^{2+} + Al^{3+}$ (Belperio et al. 2007). A similar model was postulated following experiments carried out by (Budzyń et al. 2017). The differences in the chemical composition of the two allanite populations are also clearly observed on the Raman spectra. The banks of the RS for the second allanite population are shifted toward higher energies than those of the first population (Figures 9 and 10).

Based on the replacement model proposed in publications by Li and Zhou (Li and Zhou 2017) and Li et al. (Li et al. 2018), the mass balance calculations are difficult in the case of hydrothermal processes. Ce-chevkinite, described in detail in the above-mentioned publications, contains high total levels of REE and TiO_2, and low total levels of Fe and SiO_2, and a total absence of alumina. In the vicinity of allanite grains, no Ti-oxides are observed, and replacement textures are commonly lacking. Based on these observations, it can be suggested that crystalization of the allanites and chevkinite took place during different stages

of the deposit development. The first population of allanite (older) was formed during the early stages of alteration (841–836 Ma) (stage II) while the second (younger) was established during the later hydrothermal processes (575–430 Ma) (stage III) (Zhao and Zhou 2011; Pieczonka et al. 2019). A temperature of 355°C let to explain the position of the second allanite stage (Li and Zhou 2018). The major volume of allanite is correlated with the precipitation of magnetite (Li and Zhou 2018). Association of both second allanite and magnetite minerals has been confirmed also in the our previous publications (575–430 Ma) (Pieczonka et al. 2019). This age is also confirmed by presence of REE within the magnetite. Both allanite populations confirmed the presence of different stages and the possible late crystallization of REE containing mineral phases (Petrik et al. 1995; Pieczonka et al. 2017, 2019). The patterns of REE of the two populations of allanites (Figure 12) are similar; however, the second population has a clearly visible negative Ce anomaly. Both populations are characterized by positive Ho, Tb and Lu anomalies.
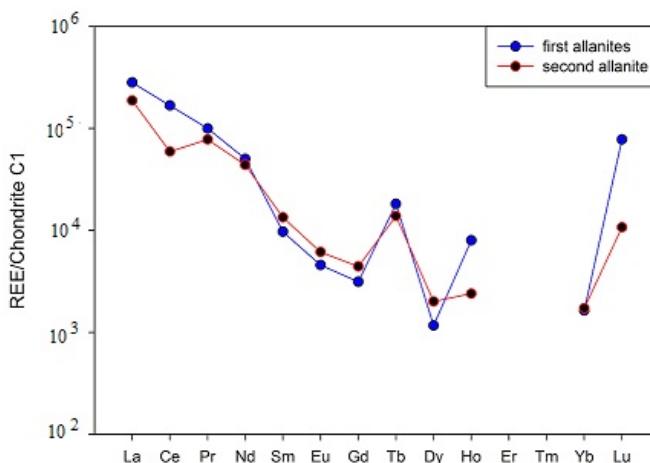

Fig. 12. Curves of the average content of REE metals, two allanite populations,
normalized to their content in C1 chondrite

Rys. 12. Krzywe średnich zawartości metali REE w dwóch populacjach allanitu,
znormalizowanych do ich zawartości w chondrycie C1

Differences in REE patterns of the host rocks (Figure 4) and separate allanites (Figure 12) can also suggest fluid circulation over time that results in chemical composition of both allanite populations. However, the REE patterns in Figure 4 are smooth. This is connected with REE broad dispersion in the host rocks which took place during hydrothermal alteration. Hydrothermal alteration of the host rocks happened during the cooling of fluids responsible for ions transportation and mineral crystallization. A temperature of 355°C might be an initial temperature of the final crystallization of minerals which were recognized as a polymetallic stage.

The distributions of REE and the main metal oxide compositions: CaO, Al_2O_3, FeO, SiO_2 are shown in Figures 13A, 13B, 13C, 13D and 13E, respectively. Apart from silica, all the major elements including REE show a clearly visible bi-modal distribution on the histograms (Figure 13A–D). Silica, having comparable amounts in both populations, the uni-modal characteristic (Figure 13E) and very low coefficient of variability (4.1 and 3.7, rf. Tables 2a and 2b), characterizes a more stable element in the allanite structure.
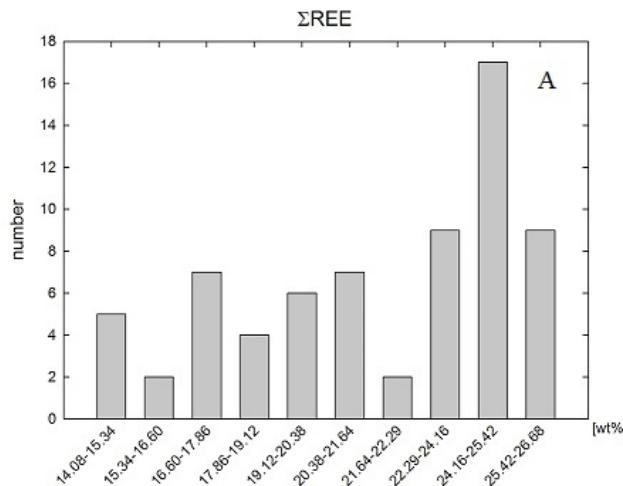
Fig. 13A. Histogram of REE content in allanites

Rys. 13A. Histogram zawartości REE w allanitach
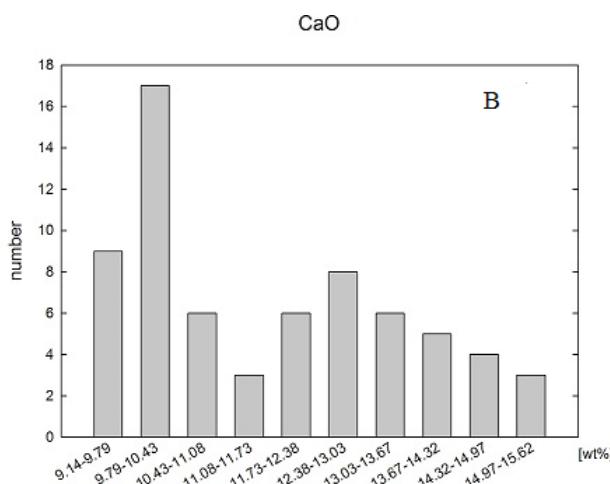
Fig. 13B. Histogram of CaO content in allanites

Rys. 13B. Histogram zawartości CaO w allanitach
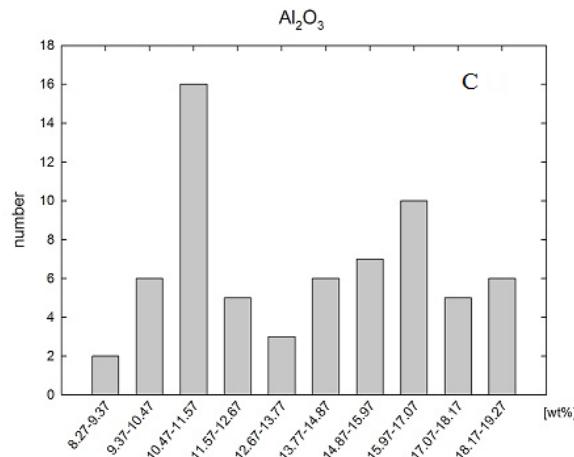
Fig. 13C. Histogram of Al$_2$O$_3$ content in allanites

Rys. 13C. Histogram zawartości Al$_2$O$_3$ w allanitach
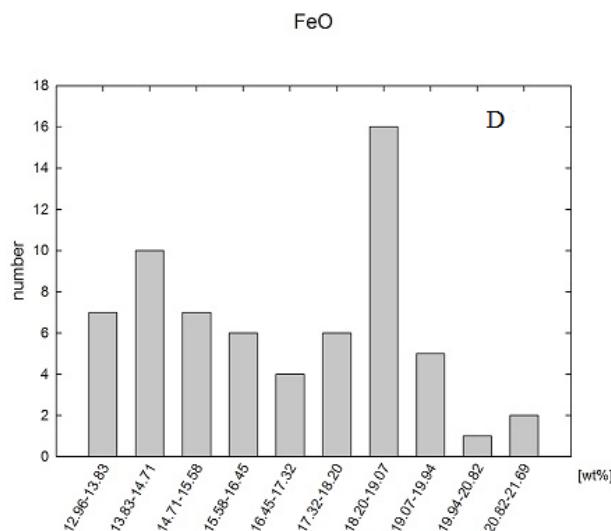
Fig. 13D. Histogram of FeO content in allanites

Rys. 13D. Histogram zawartości FeO w allanitach
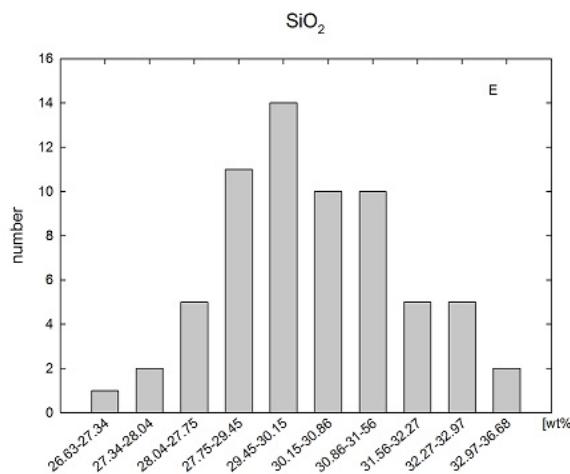
Fig. 13E. Histogram of SiO_2 content in allanites

Rys. 13. Histogram zawartości SiO_2 w allanitach

4.2. Other minerals responsible
for the accumulation of REE

The balance of REE in the deposit is based on the bulk chemical analyses and WDS point measurements as well as mineralogical observation. The following minerals are responsible for the accumulation of REE: allanite, titanite, apatite, monazite, uraninite and epidote. Only the first two are distributed within the ore to have significant impact on REE concentration. Allanite as a mineral commonly occurring in the deposit containing the highest concentrations of REE is their most important carrier. This mineral is collected from the waste pond at the end of the technological process (Pieczonka et al. 2019).

Titanite is a common mineral in the ore. It formed elongated crystals of up to 500 μm and occurs on the level similar to the allanite. The concentration of REE in titanites ranges from 0.121% up to 2.722% with an average of 0.866% (Table 4). The coefficient of variability (71%) shows distinct variation in the chemical composition. It is well visible on BSE images (Figure 14A–D) showing different shadows within the titanite grains, which are dependent on REE concentrations. Big titanite crystals are cemented by the epidote- pyroxene-chloride matrix and reveal mosaic internal building which occurs as a result of recrystallization which took place in the past. REE chondrite normalized pattern of host rocks (Figure 4) and of titanite (Figure 15) show significant differences. It can be concluded that titanite participate in association at the end of REE mineral member crystallization (Pieczonka et al. 2018).

Table 4.   WDS composition of titanites, sample W-25 from Sin Quyen deposit

Tabela 4.   Skład chemiczny tytanitów, próba W-25 ze złoża Sin Quyen, analiza WDS

No.	F	Na₂O	MgO	Al₂O₃	SiO₂	CaO	TiO₂	MnO	FeO	ZrO₂	Nb₂O₅	SnO₂	HfO₂	Ta₂O₅	PbO	ThO₂
1	1.057	0.027	b.d.l.	2.616	30.788	28.141	30.062	b.d.l.	2.854	0.029	2.883	0.065	0.021	b.d.l.	b.d.l.	b.d.l.
2	1.290	0.020	0.089	2.108	30.167	27.010	29.149	b.d.l.	4.691	b.d.l.	1.543	0.064	b.d.l.	b.d.l.	b.d.l.	0.019
3	0.960	0.006	0.011	2.828	30.359	27.644	31.124	0.043	2.301	0.022	2.323	0.104	b.d.l.	0.045	b.d.l.	b.d.l.
4	0.947	b.d.l.	0.032	2.930	30.834	28.256	30.097	0.028	3.834	b.d.l.	2.237	0.084	b.d.l.	0.039	b.d.l.	0.011
5	0.445	b.d.l.	b.d.l.	1.660	31.377	29.036	35.695	0.052	1.347	b.d.l.	1.068	b.d.l.	b.d.l.	b.d.l.	b.d.l.	b.d.l.
6	0.446	b.d.l.	0.029	1.239	30.228	27.575	34.847	0.022	2.715	b.d.l.	0.197	0.054	b.d.l.	b.d.l.	b.d.l.	0.011
7	0.239	0.004	0.025	1.112	30.030	27.076	34.729	0.033	2.215	b.d.l.	0.240	0.100	0.053	b.d.l.	0.015	0.024
8	0.102	0.100	0.037	1.133	30.099	26.367	31.691	0.022	3.336	b.d.l.	3.510	0.164	b.d.l.	0.032	b.d.l.	0.017
9	0.699	0.004	0.022	2.474	30.615	27.944	32.259	0.037	2.184	b.d.l.	2.069	0.246	0.057	b.d.l.	b.d.l.	b.d.l.
10	0.599	b.d.l.	b.d.l.	2.950	30.971	28.423	32.413	0.027	1.165	b.d.l.	2.155	0.216	b.d.l.	b.d.l.	b.d.l.	b.d.l.
11	0.700	0.015	b.d.l.	2.390	30.845	27.984	32.279	0.040	2.146	b.d.l.	1.936	0.225	b.d.l.	b.d.l.	b.d.l.	0.013
12	0.876	b.d.l.	0.022	2.712	30.810	28.302	32.381	0.046	2.061	b.d.l.	1.749	0.162	b.d.l.	b.d.l.	b.d.l.	b.d.l.
13	0.605	0.056	0.038	1.004	30.680	28.434	35.958	0.045	2.271	b.d.l.	0.139	0.025	0.013	b.d.l.	b.d.l.	0.024
14	0.742	0.030	0.018	2.402	30.900	28.180	32.158	0.052	2.200	b.d.l.	1.981	0.238	b.d.l.	b.d.l.	b.d.l.	b.d.l.
15	0.779	b.d.l.	0.010	2.718	30.931	28.346	33.342	0.028	1.374	b.d.l.	1.438	0.177	0.012	0.074	0.011	b.d.l.
16	0.618	b.d.l.	0.022	2.399	30.617	27.804	32.178	0.055	2.237	b.d.l.	2.066	0.239	b.d.l.	0.045	0.013	b.d.l.
17	0.962	0.010	0.027	2.680	30.502	28.061	30.824	0.037	3.147	b.d.l.	2.157	0.213	b.d.l.	b.d.l.	b.d.l.	b.d.l.
18	0.708	0.010	0.014	3.033	31.069	28.494	33.029	0.033	0.967	0.010	1.966	0.249	0.094	b.d.l.	b.d.l.	b.d.l.
19	0.708	b.d.l.	0.023	2.303	30.450	27.985	32.709	0.023	1.717	0.047	1.861	0.238	b.d.l.	0.027	b.d.l.	b.d.l.
21	0.718	b.d.l.	0.014	2.401	30.754	28.170	32.556	0.037	2.201	b.d.l.	1.747	0.151	0.014	b.d.l.	b.d.l.	b.d.l.
22	1.136	0.010	0.011	3.205	31.032	28.630	31.372	0.031	2.438	b.d.l.	1.593	0.270	0.025	0.020	0.017	b.d.l.
23	0.275	b.d.l.	b.d.l.	1.931	30.907	28.662	33.282	0.055	1.296	b.d.l.	3.972	b.d.l.	0.031	b.d.l.	b.d.l.	b.d.l.
24	1.084	b.d.l.	0.028	3.324	30.979	28.379	29.923	0.038	3.105	b.d.l.	2.008	0.328	b.d.l.	b.d.l.	b.d.l.	b.d.l.
25	0.857	0.013	0.030	2.707	30.744	28.127	31.143	0.026	2.850	0.047	1.786	0.323	b.d.l.	b.d.l.	0.026	b.d.l.
26	0.223	0.024	b.d.l.	1.793	30.761	28.764	33.172	0.049	1.254	b.d.l.	4.053	b.d.l.	0.019	0.061	b.d.l.	0.010
27	1.028	b.d.l.	0.010	2.875	30.362	28.235	30.854	0.019	3.161	0.032	1.858	0.299	0.039	b.d.l.	b.d.l.	b.d.l.
28	1.122	b.d.l.	0.022	3.795	30.977	28.368	30.119	0.044	2.557	b.d.l.	1.661	0.204	b.d.l.	b.d.l.	0.019	b.d.l.
29	0.889	b.d.l.	0.004	2.531	30.773	28.478	31.176	0.031	3.075	b.d.l.	1.978	0.177	0.015	0.003	b.d.l.	b.d.l.
30	1.188	0.013	0.065	3.066	30.755	27.750	29.995	0.020	3.723	b.d.l.	1.430	0.071	b.d.l.	b.d.l.	b.d.l.	0.017

No.	Y_2O_3	La_2O_3	Ce_2O_3	Nd_2O_3	Sm_2O_3	Gd_2O_3	Dy_2O_3	Er_2O_3	Lu_2O_3	$\sum REE_2O_3$	Total	Comment
1	0.067	0.054	0.257	0.114	0.035	0.012	0.032	b.d.l.	b.d.l.	0.504	98.674	Ap499_fot5_p1
2	0.615	0.140	0.664	0.595	0.141	0.038	0.079	0.065	b.d.l.	1.722	97.944	Ap499_fot5_p2
3	0.298	0.049	0.422	0.323	0.076	0.039	0.094	0.032	b.d.l.	1.035	98.699	Ap499_fot5_p3
4	0.303	0.047	0.346	0.260	0.051	0.014	0.069	0.030	0.001	0.818	100.05	Ap499_fot8_p1
5	b.d.l.	0.031	0.079	b.d.l.	b.d.l.	0.011	b.d.l.	b.d.l.	b.d.l.	0.121	100.62	Ap499_fot8_p2
6	0.203	0.345	1.172	0.853	0.120	0.004	0.073	0.031	b.d.l.	2.598	99.976	Ap499_fot9_p1
7	0.316	0.289	1.382	0.753	0.112	0.030	0.076	0.055	b.d.l.	2.697	98.807	Ap499_fot11_p1
8	0.636	0.266	1.145	0.872	0.173	0.025	0.137	0.061	0.043	2.722	99.925	Ap499_fot12_p1
9	0.381	0.073	0.272	0.210	0.039	0.023	0.092	0.034	0.003	0.746	99.451	Ap499_fot6_p2
10	0.237	b.d.l.	0.102	0.042	0.013	b.d.l.	0.067	0.008	0.012	0.244	99.181	Ap499_fot6_p3
11	0.344	0.037	0.366	0.180	0.051	0.008	0.081	0.048	0.014	0.785	99.427	Ap499_fot7_p1
12	0.234	0.143	0.317	0.244	0.048	0.015	0.069	0.010	0.006	0.852	99.848	Ap499_fot7_p2
13	0.058	0.203	0.398	0.086	b.d.l.	0.034	0.037	b.d.l.	0.013	0.771	99.866	Ap499_fot7_p3
14	0.333	0.018	0.286	0.198	0.041	0.015	0.072	0.025	b.d.l.	0.655	99.577	Ap499_fot8_p3
15	0.191	0.011	0.343	0.151	0.032	0.021	0.047	0.024	0.005	0.634	99.737	Ap499_fot8_p4
16	0.327	0.032	0.285	0.185	0.052	b.d.l.	0.067	0.025	0.031	0.677	99.039	Ap499_fot8_p5
17	0.169	0.005	0.257	0.215	0.039	b.d.l.	0.043	0.037	b.d.l.	0.596	98.996	Ap499_fot9_p2
18	0.190	b.d.l.	0.211	0.152	0.048	0.044	0.038	0.044	0.035	0.572	100.14	Ap499_fot9_p3
19	0.367	0.081	0.441	0.175	0.037	b.d.l.	0.077	0.029	b.d.l.	0.840	99.000	Ap499_fot9_p4
21	0.333	0.057	0.437	0.343	0.086	b.d.l.	0.080	0.056	b.d.l.	1.059	99.869	Ap499_fot9_p6
22	0.141	0.066	0.181	0.156	0.053	b.d.l.	0.052	0.049	b.d.l.	0.557	100.01	Ap499_fot10_p1
23	0.006	b.d.l.	0.067	0.018	0.024	0.007	0.029	b.d.l.	b.d.l.	0.145	100.45	Ap499_fot10_p2
24	0.182	b.d.l.	0.255	0.198	0.001	b.d.l.	0.065	0.019	b.d.l.	0.538	99.469	Ap499_fot10_p3
25	0.406	0.112	0.349	0.103	0.063	b.d.l.	0.080	0.058	b.d.l.	0.765	99.493	Ap499_fot10_p4
26	b.d.l.	b.d.l.	0.098	0.057	b.d.l.	b.d.l.	0.021	0.030	b.d.l.	0.206	100.31	Ap499_fot10_p5
27	0.467	0.085	0.362	0.217	0.033	b.d.l.	0.091	0.005	b.d.l.	0.793	99.601	Ap499_fot10_p6
28	0.303	0.058	0.208	0.202	0.075	b.d.l.	0.060	0.047	0.010	0.660	99.388	Ap499_fot10_p7
29	0.173	0.063	0.260	0.204	0.091	b.d.l.	0.055	0.046	0.005	0.724	99.659	Ap499_fot10_p8
30	0.527	0.127	0.407	0.343	0.072	0.016	0.130	0.021	b.d.l.	1.116	99.239	Ap499_fot11_p2

Table 4.   cont.

Tabela 4.   cd.

No.	F	Na₂O	MgO	Al₂O₃	SiO₂	CaO	TiO₂	MnO	FeO	ZrO₂	Nb₂O₅	SnO₂	HfO₂	Ta₂O₅	PbO	ThO₂
31	1.077	b.d.l.	0.035	3.092	30.941	28.432	30.543	0.040	3.517	b.d.l.	1.283	0.071	b.d.l.	0.025	b.d.l.	b.d.l.
32	0.746	0.015	0.023	1.639	30.954	28.397	35.260	0.030	1.827	b.d.l.	0.092	0.029	b.d.l.	b.d.l.	b.d.l.	0.018
33	0.691	b.d.l.	0.023	2.280	30.699	28.077	32.609	0.074	2.163	b.d.l.	1.955	0.224	b.d.l.	b.d.l.	b.d.l.	b.d.l.
34	1.150	b.d.l.	0.043	3.121	30.747	28.248	30.103	0.029	3.600	b.d.l.	1.279	0.100	0.008	0.025	0.013	b.d.l.
35	1.279	b.d.l.	0.031	3.564	30.968	28.134	30.322	0.003	2.774	b.d.l.	1.489	0.166	0.038	0.048	0.002	0.014
36	0.429	b.d.l.	b.d.l.	1.678	30.803	28.905	34.988	0.029	1.293	b.d.l.	1.754	b.d.l.	0.059	b.d.l.	0.017	b.d.l.
37	0.793	0.022	0.035	2.400	30.856	28.260	32.748	0.025	2.162	0.020	1.977	0.222	b.d.l.	0.035	b.d.l.	b.d.l.
38	0.859	0.036	0.022	1.521	30.903	28.901	35.095	0.019	2.438	b.d.l.	0.004	0.030	b.d.l.	0.046	b.d.l.	0.013
39	1.405	0.020	0.079	3.113	30.630	27.966	29.601	0.016	3.787	b.d.l.	1.863	0.092	0.042	0.019	b.d.l.	0.012
ppm	282	151	169	242	208	162	225	229	327	219	225	273	462	444	254	148
Min.	0,102	0	0	1,004	30,03	26,367	29,149	0	0,967	0	0,004	b.d.l.	0	0	0	0
Max.	1,405	0,1	0,089	3,795	31,377	29,036	35,958	0,074	4,691	0,047	4,053	0,328	0,094	0,074	0,026	0,024
Av.	0,8008	0,0118	0,0239	2,4402	30,7320	28,1564	32,1522	0,0327	2,4732	0,006	1,7711	0,1479	0,0147	0,0154	0,0042	0,0068
St.d.	0,3149	0,0193	0,0200	0,7014	0,2870	0,5239	1,8621	0,0152	0,8684	0,013	0,9067	0,0981	0,0222	0,0205	0,0070	0,0074

Note: Sought but not detected: U, Yb, Pr, Tb, Tm, Ho, Eu; b.d.l. – below detection limit; Av. – average content; St.d. – standard deviation, V – coefficient of variability.

The concentration of REE in uraninites is relatively high and ranges from 1.311% up to 7.959% with an average of 4.852% for n = 33 (Pieczonka et al. 2019). However, this mineral occurring in low quantities and can be omitted from the balance of REE metals.

Epidote and ferri-epidote were identified using both optical observations and windows program calculations based on WDS quantitative measurements (Yavuz and Yildirim 2018). Both of these minerals which are members of the clinozoisite subgroup (Ambuster et al. 2006) are characterized with a variable chemical composition of major elements and very low REE content. Several tens of quantitative epidote measurements reveal only a single value which is barely above the detection limit, the rest are below the detection limit, and that is different for various metals and ranges between 642 ppm (for Ce) and 273 ppm (Sm). Low REE content in epidotes confirms a small share of these minerals in the REE balance.

No.	Y_2O_3	La_2O_3	Ce_2O_3	Nd_2O_3	Sm_2O_3	Gd_2O_3	Dy_2O_3	Er_2O_3	Lu_2O_3	$\sum REE_2O_3$	Total	Comment
31	0.248	0.061	0.318	0.287	0.078	0.027	0.053	0.044	0.012	0.880	99.737	Ap499_fot11_p3
32	0.156	0.014	0.473	0.326	0.047	b.d.l.	0.015	0.012	b.d.l.	0.887	99.770	Ap499_fot11_p4
33	0.343	0.066	0.341	0.159	0.040	b.d.l.	0.069	0.065	0.016	0.756	99.606	Ap499_fot11_p5
34	0.469	0.132	0.394	0.308	0.057	0.001	0.125	0.044	0.014	1.075	99.526	Ap499_fot12_p2
35	0.325	0.013	0.281	0.205	0.073	0.039	0.073	b.d.l.	0.005	0.689	99.311	Ap499_fot13_p1
36	b.d.l.	b.d.l.	0.076	b.d.l.	0.015	b.d.l.	0.041	0.014	b.d.l.	0.146	99.928	Ap499_fot13_p2
37	0.363	0.101	0.341	0.193	0.053	0.021	0.084	0.012	0.005	0.810	100.41	Ap499_fot13_p3
38	0.035	b.d.l.	0.302	0.032	0.017	b.d.l.	0.006	0.044	b.d.l.	0.401	99.961	Ap499_fot13_p4
39	0.432	0.119	0.416	0.334	0.081	0.006	0.086	0.063	0.017	1.122	99.608	Ap499_fot13_p5
ppm	234	642	305	466	273	561	292	362	409	–	–	detection limit
Min.	0	0	0,067	0	0	0	0	0	0	0.121	97.944	–
Max.	0,636	0,345	1,382	0,872	0,173	0,044	0,137	0,065	0,043	2.722	100.62	–
Av.	0.2678	0,0763	0,3766	0,2446	0,0544	0,0118	0,0649	0,0312	0,0065	0.866	99.562	n = 38
St.d.	0,1652	0,0835	0,2835	0,2083	0,0383	0,0140	0,0309	0,0207	0,0105	0.619	0.558	–

The minerals which are potentially REE carriers like bastnäsite and chevkinite (Li and Zhou 2018; Petrik et al. 1995) and apatite as well as monazite occur in small quantities. The low REE content of all mentioned minerals also confirms their low participation at the total REE volume.

Thus far, all the studies related to the Sin Quyen deposit have described petrological details concerning alteration processes based on the following replacement reactions: chevkinite → allanite → aeschenite and bastnäsite, monazite → fluorapatite and allanite (Petrik et al. 1995; McLean 2001; Gas'kov et al. 2012). However the mentioned minerals (Chevkinite, aeschenite, bastnäsite, monazite and fluoapatite) occur in a significantly small quantity (Petrik et al. 1995) in comparison with the common allanite, and in addition, the other reaction mentioned above played a less important role.
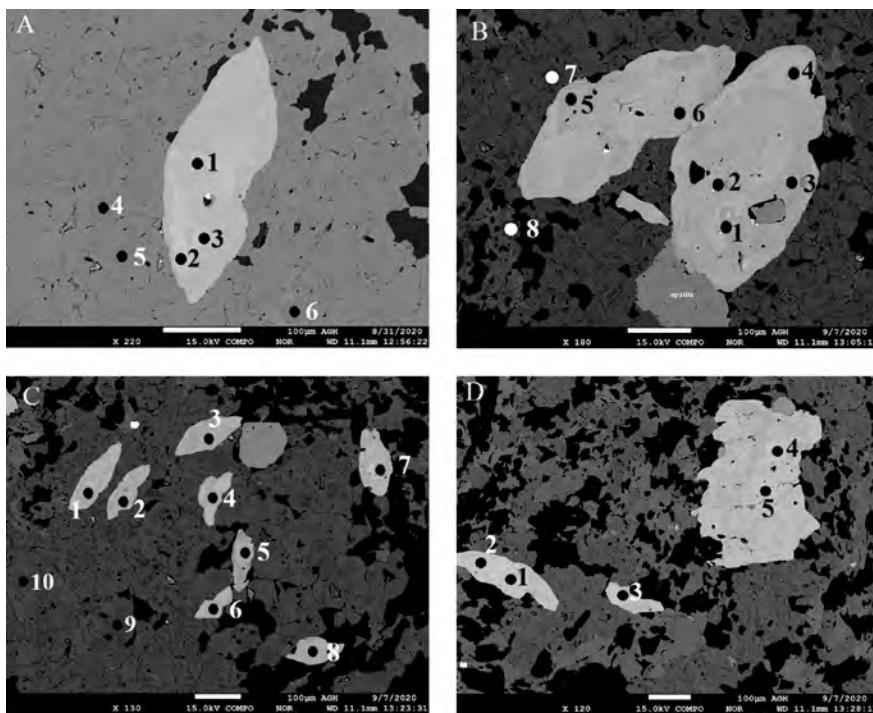
Fig. 14. BSE images of titanite – black and white dots show position of quantitative WDS measurements

Rys. 14. Obrazy BSE tytanitów, czarne i białe punkty pokazują pozycje pomiarów ilościowych WDS
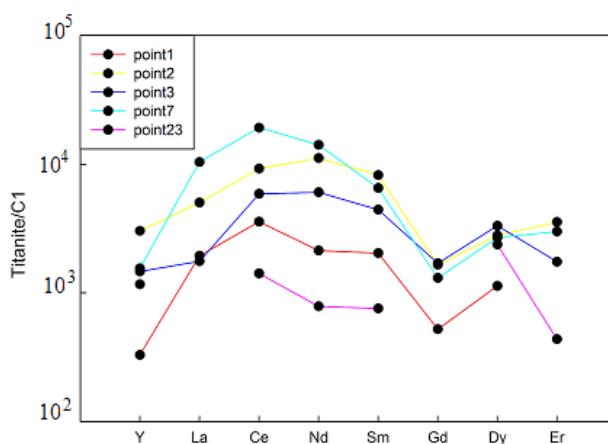
Fig. 15. The selected curves of REE contents in titanite normalized to their contents in the chondrite C1

Rys. 15. Wybrane krzywe zawartości pierwiastków REE w tytanitach znormalizowane
do ich zawartości w chondrycie C1

Conclusions

Allanites are the major carriers of the REE metals in the studied deposit. The differences in the chemical composition clearly document the presence of two populations of allanites. The first is characterized by a higher total REE_2O_3 content at the level of 20 wt% to 27 wt% and lower CaO and Al_2O_3 but higher Fe. The chemical composition of the second ferriallanite group has a low total REE_2O_3 content, which ranges from 14 to 20 wt%. In addition, negative correlations have been noted between two pairs of major compositions of the allanite: CaO and REE_2O_3, with R = –0.85 and Al_2O_3 – REE_2O_3, with R = –0.79, suggesting Ca and Al are interchangeable with REE in alteration processes. A relatively weak correlation (R = 0.60) is observed for the pair SiO_2–REE_2O_3. The visible differences between two allanite populations is clearly seen in the relationship of Ca + Fe^{3+} + Al and $\sum$REE expressed in apfu. Additionally, these differences were also clearly observed in Raman spectra. The conclusion can therefore be sound that the allanite minerals could be formed during different stages of the formation of the deposit. Currently, there is a valuable amount of REE in the exploitation waste. Excluding allanite, several minerals in the Sin Quyen deposit are characterizes with different total REE contents. However, only allanites which are a major carrier and titanites because of common occurrences are responsible for high concentrations of REE in the deposit.

REFERENCES

Armbruster et al. 2006 – Armbruster, T., Bonazzi, P., Akasaka, M., Barmanec, V., Chopin, C., Giere, R., Heuss-Assbichlier, S., Liebsciebscher, A., Menchetti, S., Pany,Y. and Pasero, M. 2006. Recommended nomenclature of epidote-group minerals. *European Journal of Mineralogy* 18(5), pp. 551–567, DOI: 10.1127/0935-1221/2006/0018-0551.

Belperio et al. 2007 – Belperio, A., Flint, R. and Freeman, H. 2007. Prediment Hill: A hematite dominated, iron oxide copper-gold system. *Economic Geology* 102, pp. 1499–1510.

Budzyń et al. 2017 – Budzyń, B., Harlov, D.E., Kozub-Budzyń, G.A. and Majka, J. 2017. Experimental constraints on the relative stabilities of the two systems monazite-(Ce)–allanite-(Ce) – fluor apatite and xenotime-(Y)––(Y.HREE)-rich epidote – (Y.HREE)-rich fluor apatite, in high Ca and Na-Ca environments under P-T conditions of 200–1000 MPa and 450–750°C. *Mineralogy and Petrology* 111, pp. 183–217, DOI: 10.1007/s00710-016-0464-0.

Carter, A. and Clift, P.D. 2008. Was the Indosinian orogeny a Triassic mountain building or a thermotectonic reactivation event?, Comptes Rendus. *Geosciences* 340(2–3), pp. 83-93, DOI: 10.1016/j.crte.2007.08.011.

Chen et al. 2015 – Chen, W.T., Zhou, M.F., Gao, J.F. and Hu, R. 2015. Geochemistry of magnetite from Proterozoic Fe-Cu deposits in the Kangdian metallogenic province, SW China. *Mineralium Deposita* 50, pp. 795–809, DOI: 10.1007/s00126-014-0575-7.

Dupuis, C. and Beaudoin, G. 2011. Discriminant diagrams for iron oxide trace element fingerprinting of mineral deposit types. *Mineralium Deposita* 46(4), pp. 319–335, DOI: 10.1007/s00126-011-0334-y.

ESCAP 1990. Report of Economic and Social Commission for Asia and the Pacific.

Faure et al. 2014 – Faure, M., Lepvrier, C., Vuong, N.V., Tich, V.V., Lin, W. and Chen, Z. 2014. The South China block-Indochina collision: Where, when, and how? *Journal of Asian Earth Sciences* 79, pp. 260–274, DOI: 10.1016/j.jseaes.2013.09.022.

Fengli et al. 2014 – Fengli, Y., Yafei, W., Shinfu, L., Xiaofen, L., Pengfei, G. and Jiannian, Z. 2014. Comparisons between the Zhuchong Fe-Cu Deposit in Anqing and the IOCG-type Deposits. *Acta Geologica Sinica* 88(S2), pp. 403–404, DOI: 10.1111/1755-6724.12372_28.

Gas'kov et al. 2012 – Gas'kov, V., Tran, T.A., Tran, T.H., Pham, T.D., Nevolko, P.A. and Pham, N.C. 2012. The Sin Quyen Cu-Fe-Au-REE deposit (*northern Vietnam*) composition and formation conditions. *Russian Geology and Geophysics* 53(5), pp. 442–456, DOI: 10.1016/j.rgg.2012.03.005.

Hao et al. 2021 – Hao, D.V., Phan, T.T., Nguyen, D.T., Piestrzyski, A., Chau, N.D., Pieczonka, J., Ngo, X.D., Tran, V. P., Pham, T.B., Nguyen, V.H., Ngo, V.L., Bui, T.D., Vu, K.D. and Bui, T. C. 2021. Cu-Au mineralization of the Sin Quyen deposit in North Vietnam: a product of Cenozoic left-lateral movement along the Red River shear zone. *Ore Geology Reviews* 132, pp. 1–21, DOI: 10.1016/j.oregeorev.2021.104065.

Hao et al. 2021a – Hao, D.V., Chau, N.D., Piestrzyński, A. and Pieczonka, J. 2021. Relationship between Selected Major, Minor, and Trace Elements in Iron Oxide–Copper–Gold Deposits, an Example from the Unique Sin Quyen Deposit (Lào Cai Province, North Vietnam). *Russian Geology and Geophysics* 62(11), pp. 1214–1228, DOI: 10.2113/RGG20194156.

Hezarkhani, et al. 1999 – Hezarkhani, A., Williams-Jones, A.E. and Gammons, C.H. 1999. Factor controlling a copper solubility and chalcopyrite deposition in the Sungun porphyry copper deposit, Iran. *Mineralium Deposita* 34, pp. 770–783, DOI: 10.1007/s001260050237.

Hitzman, M.W., 2000. *Iron oxide-Cu-Au deposits: what, where, when, and why*. [In:] Porter, T.M. (ed.), *Hydrothermal iron oxide copper–gold & related deposits: a global perspective*. Adelaide: PGC, pp. 9–25.

Ishihara et al. 2011 – Ishihara, S., Hideo, H., Mihoko, H., Pham, N.C., Pham, T.D. and Tran, T.A. 2011. Mineralogical and chemical characteristics of the allanite-rich copper and iron ores from the Sin Quyen mine, northern Vietnam. *Bulletin of the Geological Survey of Japan* 62(5/6), pp. 197–209, DOI: 10.9795/bullgsj.62.197.

Kuśnir, I. 2000. Mineral resources of Vietnam. *Acta Montanistica Slovaca* 2, pp. 165–172.

Landtwing et al. 2005 – Landtwing, M.R., Pettke, T., Halter, W.E., Heirich, C.A., Redmond, P.B., Einaudi, M.T. and Kuznek, K. 2005. Copper deposition during quartz dissolution by cooling magmatic-hydrothermal fluid. The Bingham porphyry. *Earth and Planetary Science Letters* 235, pp. 229–243, DOI: 10.1016/j. epsl.2005.02.046.

Leloup et al. 2007 – Leloup, P.H., Tapponnier, P. and Lacassin, R. 2007. Discussion on the role of the Red River shear zone, Yunan and Vietnam in the continental extrusion of SE Asia. *Journal of Geological Society* 164, pp. 1253–1260.

Lepvrier et al. 2008 – Lepvrier, C., Maluski, H., Nguyen, V.V., Roques, D., Axente, V. and Rangin, C. 2008. Indosinian NW-trending shear zones within the Truong Son belt (Vietnam), [40]Ar-[39]Ar Triasic age and Cretaceous to Cenozoic overprints. *Tectonophysics* 283, pp. 105–127, DOI: 10.1016/S0040-1951(97)00151-0.

Li, X.C. and Zhou, M.F. 2017. Hydrothermal alteration of monazite-(Ce) and chevkinite-(Ce) from the Sin Quyen Fe-Cu-LREE-Au deposit, northwestern Vietnam. *American Mineralogists* 102(7), pp. 1525–1541, DOI: 10.2138/am-2017-5970.

Li, X.C. and Zhou, M.F. 2018. The nature and origin of hydrothermal REE mineralization in the Sin Quyen deposit, Northwestern Vietnam. *Economic Geology* 113(3), pp. 645–673, DOI: 10.5382/econgeo.2018.4565.

Li et al. 2018 – Li, X.C., Zhou, M.F., Chen, W.T., Zhao, X.F. and Tran, M.D. 2018. Uranium-lead dating of hydrothermal zircon and monazite from the Sin Quyen Fe-Cu REE-Au-(U) deposit, northwestern Vietnam. *Mineralium Deposita* 53(3), pp. 399–416, DOI: 10.1007/s00126-017-0746-4.

Liem et al. 2016 – Liem, N.V., Dat, N.P., Dieu, B.T., Phai, V.V., Trinh, P.T., Vinh, H.Q. and Phong, T.V. 2016. Assessment of geomorphic processes and active tectonics in Con Voi mountain range area (Northern Vietnam) using the hypsometric curve analysis method. *Vietnam Journal Earth Sciences* 38(2), pp. 202–216, DOI: 10.15625/0866-7187/38/2/8602.

López, A. and Frost, R.L. 2015. Identification of allanite (Ce, Ca, Y)2(Al, Fe3+)3(SiO4)3OH found in marble from Chillagoe, Queensland using Raman spectroscopy. *Spectrochimica Acta Part A: Molecular and Biomolecular Spectroscopy* 138, pp. 229–233, DOI: 10.1016/j.saa.2014.11.052.

McLean, R.N. 2001. *The Sin Quyen iron oxide-copper-gold-rare earth oxide mineralization of North Vietnam*. [In:] Porter, T.M. (ed.), *Hydrothermal iron oxide copper-gold & related deposits: A global perspective.* Adelaide: PGC, pp 293–301.

Ngo et al. 2020 – Ngo, X.D., Zhao, X.F., Tran, T.H., Deng, X.D. and Li, J.W., 2020. Two episodes of REE mineralization of the Sin Quyen IOCG deposit, NW Vietnam. *Ore Geology Reviews* 125, DOI: 10.1016/j.oregeorev.2020.103676.

Ohmoto, H. and Rye, R.O. 1979. *Isotopes of sulfur and carbon*. [In:] Barnes, H.L. (ed.), *Geochemistry of hydrothermal ore deposits 2nd*. New York, pp. 509–567.

[Online:] http://webmineral.com/data/Ferriallanite-(Ce).shtml#.X8UMq2hKhaQ.

Petrik et al. 1995 – Petrik, I., Broska, I., Lipka, J. and Siman, P. 1995. Granitoid Allanite-(Ce) substitution relations, redox conditions and REE distributions (on an Example of I-Type Granitoids, Western Carpathians, Slovakia). *Geologia Carpathica* 46, pp. 79–94.

Pham et al. 2011 – Pham, N.C., Ishiyama, D., Tran, T.A. and Sera, K. 2011. Mineralogical and geochemical characteristics of rare metals bearing Na Bop, Lung Hoai, Nason and Sin Quyen Base metal deposits, Northern Vietnam. *NMCC Annual Report* 18, pp. 49–55.

Pieczonka et al. 2019 – Pieczonka, J., Piestrzyński, A., Chau, N.D. and Phon, L.K. 2019. Timing of ore mineralization using ore mineralogy and U-Pb dating, Iron Oxide Copper Gold Sin Quyen deposit, North Vietnam. *Geological Quarterly* 63(4), pp. 861–874, DOI: 10.7306/gq.1507.

Pieczonka et al. 2017 – Pieczonka, J., Piestrzyński, A., Phon, L.K., Chau, N.D. and Hao, D.V. 2017. IOCG Sin-Quyen deposit, Lao Cai, N-Vietnam. Mineral resources to discover. *14th Biennial SGA Meeting*, Quebec, Canada, pp. 955–959.

Pieczonka et al. 2015 – Pieczonka, J., Piestrzyński, A., Phon, L.K., Chau, N.D., Jodłowski, P. and Hao, D.V. 2015. Rare Earth, radioactive and selected elements in the iron oxide copper gold Sin Quyen deposit in North Vietnam. *Second International Conference on Scientific Research Cooperation between Vietnam and Poland in Earth Sciences*. Bach Khoa Publishing Mouse, Hanoi, pp. 331–353.

Pyle et al. 2002 – Pyle, J.M., Spear, F.S. and Wark, D.A. 2002. Electron microprobe analysis of REE in apatite, monazite and xenotime: protocols and pitfalls. *Mineralogy and Geochemistry* 48(1), pp. 337–362, DOI: 10.2138/rmg.2002.48.8.

Seal, R. 2006. Sulphur isotope geochemistry of sulphide minerals. *USGS Staff – Published Research* 345. [Online] https://digitalcommons.unl.edu/usgsstaffpub/345.

Shieh, R.S. and Duffy, T.S. 2002. Raman spectroscopy of Co(OH)2 at high pressures: Implications for amorphization and hydrogen repulsion. *Physical Review B* 66(13), pp. 1–8, DOI: 10.1103/PhysRevB.66.134301.

Roger, et al. 2012 – Roger, F., Maluski, H., Lepvrier, C., Vu, V.T. and Paquette, J.L. 2012. LA-ICPMS zircons U/Pb dating of Permo-Trassic and Cretaceous magmatism in Northern Vietnam – Geodynamical implications. *Journal of Asian Earth Sciences* 48, pp. 72–82, DOI: 10.1016/j.jseaes.2011.12.012.

Ta, V.D. 1975. *Report of geological surveys and their results performed at the IOCG Sin Quyen deposit in Lao Cai, North Vietnam*. Main Department of Geology of Vietnam. 318 (*in Vietnamese*).

Tapponnier et al. 1990 – Tapponnier, P., Lacassin, R., Leloup, H., Scharer, U., Zhong, D., Liu, X., Ji, S., Zhang, L. and Zhong, J. 1990. The Ailaoshan-Red river metamorphic belt: tertiary left-lateral shear between Indochina and South China. *Nature* 343, pp. 431–437, DOI: 10.1038/343431a0.

Tong et al. 1996 – Tong, D.T., Javier, P. and Ta, H.P. 1996. Fist suggest continental connections between the Indochina and South China blocks in Middle Devonian time. *Geology* 24, pp. 571–574, DOI: 10.1130/0091-7613(1996)024<0571:FSCCBT>2.3.CO;2.

Yavuz, F. and Yildirim, D.K. 2018. A windows program for calculation and classification of epidote-supergroup minerals. *Periodico di Mineralogia* 87, pp. 269–285.

Zhao, X.F. and Zhou, M.F. 2011. Fe-Cu deposits in the Kangdian region, SW China: a Proterozoic IOCG (iron-oxide–copper–gold) metallogenic province. *Mineralium Deposita* 46 (7), pp. 731-747, DOI: 10.1007/s00126-011-0342-y.

RARE EARTH ELEMENTS IN THE SIN QUYEN IOCG DEPOSIT, NORTH VIETNAM

A b s t r a c t

The Sin Quyen deposit is characterized by a high accumulation of rare earth elements (REE). This deposit belongs to the IOCG type copper deposits (Iron Oxide Copper-Gold Deposits). In the deposit, the REE carrier minerals have been identified as follow: allanite, titanite, uraninite, monazite, apatite, chevkinite, aeschynite, bastnäsite, and epidote. In the skarn zone, contents of allanite range from single percentages to 10% in hand-size specimens. Locally, minerals of epidote subgroup which occur in large amounts in the host rocks are important. The studied allanites have concentrations of: REE (14–27 wt%), Ca (9–16 wt%), Al (8–19 wt%), Si (26–34 wt%) and Fe (12–21 wt%). Two populations of allanite are documented, the first is texturally older and probably related to the Ca-K alteration (second stage of crystallization). This population has higher REE concentration ranging from 20 to 27 wt%. The second population is texturally younger and has a lower total REE concentration ranging from 14 to 19.9 wt%, which occur mostly as a rim surrounding the older and likely arose during the K alteration with Cu-Au mineralization (third crystallization). The chemical composition indicates that the studied allanites belong to the Ce-La-ferriallanite family, with low ΣHREE and an average of 0.21 wt.%. A temperature of 355°C which was calculated using a value of δ34S isotopes is interpreted as a temperature of the second crystallization stage of allanite. In the studied deposit, excluding allanite and titanite, the other bearing REE minerals have an insignificant role in the REE balance, since they either have the total content of REE, which is often close to the WDS detection limit (rf. the epidote subgroup), or their only occur at the single points. The content of total REE in accessory uraninites is high and range from 1.311% up to 7.959% with an average value of 4.852%.

PIERWIASTKI ZIEM RZADKICH W ZŁOŻU IOCG SIN QUYEN, PÓŁNOCNY WIETNAM

S t r e s z c z e n i e

Złoże Sin Quyen charakteryzuje się wysoką zawartością pierwiastków ziem rzadkich (REE). Złoże to należy do typu złóż miedzi IOCG (*Iron Oxide Copper-Gold Deposits*). Zidentyfikowane minerały zawierające REE to: allanit, tytanit, uraninit, monacyt, apatyt, czewkinit, aeschynit, bastnäsyt i epidotyt. W próbkach wielkości dłoni, pobranych ze strefy skarnowej, zawartości allanitu wahają się od pojedynczych do 10%. Lokalnie, minerały podrzędnej grupy epidotytu są ważne z powodu ich licznego występowania. Badane allanity zawierają: REE (14–27 wt%), Ca (9–16% wag.),

Al (8–19% wag.), Si (26–34% wag.) i Fe (12–21% wag.). Udokumentowano dwie populacje allanitu, pierwsza jest teksturalnie starsza i prawdopodobnie związana z alteracją Ca-K (drugi etap krystalizacji). Ta populacja ma wyższe koncentracje REE, które są zawarte w przedziale od 20 do 27% wag. Druga populacja jest młodsza i zawiera mniejsze ilości ziem rzadkich (od 14 do 19,9% wag.). Populacja ta występuje głównie w postaci obwódek regeneracyjnych, tworząc zrosty ze starszą populacją i jest związana z alteracją potasową oraz mineralizacją Cu-Au (trzeci etap krystalizacji). Skład chemiczny wskazuje, że badane allanity należą do podgrupy Ce-La-ferriallanitu, o niskiej i średniej koncentracji ΣHREE 0,21% wag. Temperatura krystalizacji 355°C, została obliczona na podstawie wartości $\delta^{34}S$. Ta temperatura jest interpretowana jako temperatura drugiego etapu krystalizacji. W badanym złożu, poza allanitami i tytanitami, inne minerały REE i ich nośniki mają małe znaczenie w bilansie ich zawartości. Na przykład sumaryczna zawartość REE w podrzędnie występującym epidocie, jest na poziomie wykrywalności metody WDS, a inne minerały, takie jak uraninit, czewkinit, aeschynit, czy bastnäsyt występują zbyt rzadko, aby wpływać na bilans tych metali. W akcesorycznym uraninicie, pomierzone zawartości REE wahają się w granicach 1,31–7,96%, przy średniej zawartości 4,85%.

Appendix 1. Bulk chemical compositions of samples collected from rocks and ore (ACME lab.) (Hao et al. 2021)

Załącznik 1. Skład chemiczny próbek pobranych ze skał i złoża (ACME lab.)

Sample	Na	Mg	Al	S	K	Ca	Sc	Ti	V	Cr	Mn	Characteristics of the sampling point
unit	%	%	%	%	%	%	ppm	%	ppm	ppm	ppm	
LLD	0.01	0.01	0.01	0.02	0.01	0.01	0.02	0.001	2	0.5	1	–
M1	0.09	0.14	0.55	7.46	0.14	1.09	1.1	0.025	28	16.0	274	Ep-Am rock, Cu-Fe ore
M2	0.12	0.34	0.95	2.38	0.19	2.16	3.2	0.078	50	8.1	308	Ep-Am rock, Cu ore
M3	0.01	0.03	0.59	3.97	0.02	4.12	1.8	0.072	44	18.8	512	Ep-Am rock
M4	0.06	0.25	0.56	5.35	0.25	0.59	2.0	0.083	90	19.3	226	massive Cu-Fe ore
M5	0.02	1.71	2.03	1.14	2.30	2.58	3.3	0.141	104	20.0	528	Cu-Fe ore
M6	0.08	0.53	1.63	1.69	1.15	1.40	2.6	0.098	50	26.8	499	Bt-Am rock,Cu ore
M7	0.11	0.14	0.68	1.87	0.13	0.92	1.4	0.017	37	5.0	305	massive Fe ore
M8	0.11	0.69	2.13	2.58	0.48	2.37	3.7	0.058	69	9.6	1028	massive Cu-Fe ore
N1	0.07	2.77	2.82	0.91	2.81	0.57	7.5	0.254	41	23.4	330	Ep-Qtz-Pl rock
N2	0.16	0.61	0.88	0.06	0.58	1.51	3.7	0.069	10	12.6	137	Carbonate-Quartz rock
N3	0.01	3.39	4.81	2.15	3.87	1.99	5.5	0.241	99	50.3	791	Skarn
N4	0.17	0.59	2.16	2.52	1.11	1.29	6.2	0.148	65	36.7	583	Bt-Am rock, Cu ore
N5	0.03	1.52	2.28	1.85	2.21	1.04	11.9	0.191	112	30.0	605	Bt-Ep rock, Cu-Fe ore
N6	0.04	0.48	1.08	2.66	0.62	1.02	2.4	0.113	103	20.0	332	Cu-Fe ore
N7	0.20	0.91	1.99	1.14	0.76	1.46	3.4	0.116	87	26.9	414	Cb-Qtz rock, Cu ore
N8	0.05	2.64	3.79	1.12	2.55	0.30	6.1	0.167	67	117.0	399	Bt-Qtz-Amp rock Cu ore
N9	0.34	1.26	2.16	0.16	0.26	2.82	4.1	0.087	50	18.6	627	Amphibolite
N10	0.01	5.43	5.90	1.26	4.11	0.32	5.7	0.266	104	46.2	449	Amphibolite Cu ore
N11	0.07	1.50	2.42	2.95	0.30	1.51	2.5	0.061	78	32.5	417	Massive Cu ore
N12	0.05	1.12	3.22	0.86	2.97	0.38	3.6	0.266	87	63.8	332	Ep-Am rock, Cu-Fe ore
S1	0.03	3.35	3.57	2.22	3.30	0.46	2.4	0.199	48	25.7	521	Bt-Am schist
S2	0.03	2.57	2.19	2.23	2.84	0.49	2.2	0.116	92	4.0	240	Cu-Fe ore
S3	0.04	0.50	1.00	2.02	0.79	0.60	1.6	0.099	92	11.6	255	Massive Cu-Fe ore
S4	0.02	0.25	0.30	2.20	0.17	0.98	1.1	0.045	81	1.9	114	Massive Cu-Fe ore
S5	0.10	0.45	1.14	1.84	0.72	0.76	3.5	0.111	73	28.4	272	Cu-Fe ore
S6	0.11	0.46	0.93	2.43	0.43	1.56	2.8	0.074	73	15.8	244	Massive Cu-Fe ore
S7	0.05	0.29	0.79	0.07	0.20	0.49	2.1	0.015	67	6.9	156	Carbonate-Quartz rock
S8	0.04	0.68	1.80	1.75	1.38	0.65	3.5	0.170	15	25.9	334	Massive Cu-Fe ore
S9	0.08	0.34	0.81	2.05	0.51	0.64	1.8	0.077	138	19.1	173	Cu-Fe ore
W15	4.22	1.03	8.52	0.10	1.34	6.72	9.0	0.283	61	–	1085	ore, open pit
W18	0.56	0.55	1.50	4.19	0.22	0.55	5.0	0.075	51	–	319	massive ore
W25	1.22	1.6	6.21	1.7	0.29	3.23	22	0.303	123	–	758	epid-amph rock
W31	1.03	3.61	4.58	0.41	1.07	6.04	16	0.268	50	–	1479	Skarn
W31a	0.02	0.26	1.95	<0.02	0.02	29.1	1	0.012	74	–	1264	skarn with garnet
Min	0.01	0.03	0.30	0.02	0.02	0.30	1.00	0.01	<2	1.90	114.0	–
Max	4.22	5.43	8.52	7.46	4.11	29.10	22.00	0.30	138.00	117.00	1479.0	n = 34
Average	0.28	1.24	2.29	1.98	1.18	2.40	4.58	0.13	100.0	25.55	479.71	–
W-36	0.24	0.32	1.07	8.33	0.29	1.90	5.00	0.06	62.0	–	236	Cu-concentrate
W-37	0.42	0.42	1.35	3.62	0.37	0.53	3.00	0.12	219	–	356	Fe-concentrate
W-40	1.88	1.85	6.23	0.60	2.01	2.70	13.0	0.26	83.0	–	792	Waste
W-44	1.59	1.39	5.52	0.77	1.15	2.79	13.0	0.22	85.0	–	711	Waste out from tailing

Appendix 1. cont.

Załącznik 1. cd.

Sample	Fe	Co	Ni	Cu	Zn	Ga	Ge	Rb	Sr	Y	Nb	Ag	Cd
unit	%	ppm	ppm	ppm	ppm	ppm	ppm	ppm	ppm	ppm	ppm	ppb	ppm
LLD	0.01	0.1	0.1	0.01	0.1	0.1	0.1	0.01	0.5	0.01	0.02	2	0.01
M1	25.52	328.7	240.3	11539	40.9	4.0	0.3	2.5	8.5	6.65	0.74	508	0.18
M2	7.74	47.6	21.4	32225	85.9	5.5	0.4	4.9	48.0	20.41	1.5	1188	0.39
M3	18.34	225.3	220.7	6751	21.6	5.1	0.7	3.8	20.9	81.39	2.49	216	0.1
M4	29.14	119.7	43.4	44900	67.9	11.4	0.6	24.5	11.3	9.49	2.55	1344	0.45
M5	28.45	82.3	22.7	29700	50.3	17.8	0.8	115	102.1	17.2	2.03	1075	0.23
M6	13.36	57.2	27.4	26524	187.1	10.7	0.5	56.8	19.3	9.12	1.27	711	0.7
M7	31.35	71.8	37.0	4972	38.8	14.7	0.9	4.3	12.3	4.24	0.33	211	0.12
M8	24.28	123	58.5	10914	137.8	22.1	0.7	58.2	32.2	8.32	0.28	506	0.32
N1	4.31	24.1	18.7	8811	33.3	10.7	0.4	112.0	13.2	46.83	0.26	1034	0.12
N2	1.18	4.5	10.3	404	9.1	4.0	0.1	24.4	17.0	38.6	0.26	98	0.03
N3	12.26	74.5	43.6	7695	48.4	22.9	0.7	194.2	26.8	11.97	1.20	754	0.1
N4	13.21	57.3	23.1	16976	173.5	15.9	0.6	107.7	9.7	14.87	1.14	1475	1.46
N5	25.62	78.8	35.4	37861	118.2	16.4	0.7	114.4	16.3	13.33	1.47	1569	0.68
N6	25.97	140.4	57.1	74400	195.9	13.8	0.6	39.1	27.7	17.85	0.72	4159	1.58
N7	7.66	44.8	23.9	17769	48.4	10.6	0.4	37.8	16.4	9.57	0.37	581	0.25
N8	11.13	67.2	40.9	20614	59.1	15.0	0.3	112.0	6.6	7.43	0.34	488	0.26
N9	6.43	16.8	9.7	1302	26.4	9.1	0.4	10.3	20.6	13.91	0.27	83	0.06
N10	12.89	86.9	35.2	28309	96.4	23.1	0.3	178.5	5.7	8.2	1.11	952	0.49
N11	14.17	151.2	94.7	82400	145.8	11.7	0.3	20.4	17.8	10.17	0.43	3050	1.02
N12	20.72	41.2	18.5	11258	51.8	15.5	0.5	150.0	8.3	7.09	0.98	498	0.15
S1	10.21	61.2	45.6	3447	91.6	13.5	0.4	294.2	8.5	4.99	0.58	283	0.21
S2	21.55	128.6	32.0	21709	82.6	15.9	0.7	170.0	17.7	10.4	1.73	1668	0.72
S3	31.55	140.5	39.4	51806	182.2	13.4	0.7	59.0	8.7	11.42	1.55	2311	1.17
S4	30.60	182.2	91.3	107878	152.2	9.7	0.6	9.4	25.0	30.56	1.41	4646	0.7
S5	21.02	60	24	26150	77.9	9.6	0.5	45.0	22.2	9.55	1.95	1090	0.38
S6	21.53	139.9	51.7	76083	109.9	7.7	0.5	24.7	43.7	17.35	1.50	2939	0.57
S7	2.08	156	4.9	394	12.6	6.2	0.1	14.9	6.7	14.18	0.08	30	0.01
S8	26.06	334	28.6	19988	43.8	18.6	0.7	88.4	16.2	11.06	0.71	1844	0.11
S9	23.59	173	41	58040	104	8.1	0.4	30.8	21.4	10.18	1.59	2107	0.67
W15	2.73	1085	7.3	186	32.5	–	–	–	90.8	17	–	8	0.06
W18	>40	319	41.4	>10000	88.3	–	–	–	11.4	10	–	1836	0.41
W25	5.81	758	35.7	2935	34.1	–	–	–	128.0	66	–	139	0.11
W31	15.28	1479	9.4	3067	57.7	–	–	–	22.3	52	–	113	0.03
W31a	0.86	1264	<0.1	39	33.3	–	–	–	98.2	11	–	14	0.07
Min	0.86	114.0	4.90	39	9.10	4.00	0.10	2.50	5.70	4.24	0.08	8.00	0.01
Max	40.00	1479.0	240.30	107878	195.90	23.10	0.90	294.20	128.0	81.39	2.55	4646	1.58
Average	17.25	479.71	46.51	25668.06	80.57	12.51	0.51	72.66	28.28	18.60	1.06	1163	0.41
W-36	35.0	183	91.6	>10000	580	–	–	–	52.1	17.0	–	30900	3.31
W-37	>40	135	84.8	998	28.0	–	–	–	13.1	15.0	–	230	0.10
W-40	9.57	36.6	24.1	386	52.2	–	–	–	45.1	55.0	–	86	0.14
W-44	12.2	30.9	20.1	335	42.3	–	–	–	46.0	99.0	–	86	0.06

Appendix 1. cont.

Załącznik 1. cd.

sample	Sn	Te	Cs	Ba	Au	Tl	Pb	Bi	Th	U
unit	ppm	ppm	ppm	ppm	ppb	ppm	ppm	ppm	ppm	ppm
LLD	0.1	0.2	0.5	0.5	0.2	0.02	0.01	0.02	0.1	0.1
M1	17.8	1.53	0.22	7.0	502.6	0.06	2.79	0.98	0.9	3.1
M2	25.3	1.5	0.38	6.7	511.1	0.06	3.79	1.47	3.3	10.5
M3	67.3	1.52	0.80	4.0	107.6	0.02	4.98	1.23	1.7	7.1
M4	19.6	3.53	3.34	13.4	991.8	0.21	7.01	2.85	1.4	24.7
M5	14.8	1.71	6.72	170.0	343.5	0.57	17.53	1.22	3.0	174
M6	22.7	1.06	3.14	130.0	237.5	0.34	5.29	0.50	1.2	10.4
M7	21.1	1.15	0.41	10.9	59.3	0.03	2.49	0.28	0.5	2.2
M8	17.1	2.42	5.50	88.2	138.0	0.18	3.70	0.80	0.9	3.1
N1	17.7	0.63	10.85	197.0	657.3	0.56	1.64	1.00	8.0	6.8
N2	3.5	0.02	2.38	53.8	102.3	0.12	1.50	0.04	5.7	5.6
N3	18.1	1.04	26.32	247.0	132.3	1.28	2.38	1.40	3.3	14
N4	27.1	1.99	16.93	128.0	1204.4	0.87	3.77	1.16	3.1	19
N5	21.3	2.57	5.58	155.0	462.9	0.72	3.13	2.14	1.8	3.2
N6	37.9	5.52	2.60	80.6	12687.5	0.46	33.92	3.81	3.7	513.1
N7	20.2	0.87	3.03	112.0	727.7	0.23	1.94	0.73	1.1	8.1
N8	8.8	0.62	8.00	241.0	161.9	0.62	3.41	0.36	3.1	56.2
N9	21.6	0.08	1.36	21.3	88.9	0.07	1.31	0.05	3.9	4.2
N10	9.3	1.36	21.27	284.0	175.9	1.1	2.80	1.44	2.7	31.6
N11	20.8	4.44	2.27	34.2	18503.7	0.42	24.27	4.64	3.2	302.4
N12	5.6	1.14	14.41	364.0	598.1	0.88	3.84	0.84	2.0	31.6
S1	18.5	0.66	48.69	159.0	121.2	1.88	3.07	0.73	2.1	8.9
S2	10.4	1.32	11.22	104.0	407.8	0.72	3.56	2.36	3.2	28.1
S3	36.3	4.18	6.52	57.6	294.7	0.38	26.21	3.01	1.9	331
S4	24.1	7.13	1.01	12.9	10531.2	0.08	24.6	4.67	3.8	316.8
S5	14.0	1.54	3.61	74.8	681.2	0.21	6.09	1.16	2.7	51.7
S7	18.5	3.95	1.51	32.4	2038.6	0.22	15.53	2.31	4.2	101.2
S8	1.0	0.03	0.63	20.0	10.4	0.06	0.89	0.06	12.5	3
S9	10.7	1.41	5.71	170.0	750.1	0.53	2.14	2.34	16.2	11.6
W15	13.9	3.5	2.32	48.3	897.7	0.19	10.56	2.06	21.4	74.6
W18	–	0.05	–	154.0	3.1	–	1.76	0.07	2.2	1.17
W25	–	3.6	–	12.8	2358.2	–	5.46	2.58	2.9	56.51
W31	–	0.28	–	18.1	28.6	–	7.61	0.31	1.4	8.35
W31a	–	0.15	–	31.4	16.9	–	3.11	0.56	0.9	16.31
Min	1.00	<0.02	0.22	4.00	1.60	0.02	0.89	0.04	0.50	0.98
Max	67.30	7.13	48.69	364.00	18503.7	1.88	33.92	4.67	21.40	513.10
Average	19.48	1.89	7.47	95.58	1662.81	0.45	7.23	1.45	3.84	65.92
W-36	4.91	–	–	36.1	6490	–	40.8	5.39	2.2	20.56
W-37	0.64	–	–	36.5	148	–	3.56	1.28	2.9	22.7
W-40	0.86	–	–	189	67.3	–	4.2	1.32	8.7	30.6
W-44	0.38	–	–	104	166.7	–	5.31	1.68	11.3	62.4